공학박사 학위논문

Surface engineering of lithium metal anode for stable lithium metal battery

안정한 리튬 금속 전지를 위한 리튬 금속 표면 제어

2020 년 8 월

서울대학교 대학원

융합과학부 나노융합전공

김 현 진

Abstract

Surface engineering of lithium metal anode for stable lithium metal battery

Hyunjin Kim
Program in Nano science and Technology
The Graduate School
Seoul National University

Batteries constitute a core technology in modern society. Batteries are found in many devices, including smartphone, smart watch, laptop, and electric vehicle, all commonly used in daily life. As the demand for batteries has increased, various studies on batteries have been conducted. One of the major topics in this field is the expansion of battery capacity, which corresponds to a key consumer concern. In order to increase capacity, it is necessary to use an electrode material of high capacity. However, the graphite-based negative electrode material continues to impose various constraints in commercialized battery production. Lithium (Li) metal is emerging as a promising next-generation material for negative electrodes with its superior capacity, low electrochemical potential, and low density. Attempts have been made to use Li metal, but obstacles remain, such as stability and safety issues. Li metal is a hostless material, so instead of maintaining the solid electrolyte interphase (SEI) layer, it will continually expand volumetrically and break. Retention of a stable SEI layer is thus a key element in implementation of Li metal

as a negative electrode. Li ion flux is concentrated on the broken gap and dendrite growth, causing an internal short circuit or increasing surface resistance due to an accumulation of electrolyte decomposition, ultimately decreased cycle stability. This paper deals with three studies of SEI layer stabilization. The first part presents a method of uniformly distributing the current density by applying a 3D structure to the Li metal surface. The second part introduces a method of polymer protective coating on the Li metal surface applied by thermal curing. The third part consists of a method of imparting a lithium fluoride layer to the Li surface through thermal curing. These methods have shown to improve the stability of the Li metal surface and thus the safety of the Li metal battery.

Keywords : lithium metal anode, lithium metal battery, protective layer, artificial solid electrolyte interphase layer

Student Number : 2014-24876

Contents

List of figures

List of tables

Chapter 1 Introduction

1.1 Overview

Batteries constitute an indispensable technology, used in many electronics such as mobile phones, wireless earphones, and laptop computers. [1] With the advent of the portable devices and electric vehicles era, the importance of batteries continues to increase. In this context, the capacity of the battery is the main issue. Consumers demand batteries that last longer. In order to increase battery capacity, it is necessary to improve the electrodes. A battery is essentially composed of two electrodes (anode and cathode), separator, and electrolyte. [2] Lithium (Li) ions at the cathode are charged along with the anode to store electrical energy as chemical energy. When the device is connected to a circuit, the internal Li ions are oxidized to provide electron flow to the external circuit. [3] The electrolyte serves as a medium that transports Li ions, and the separator separate the anode and cathode during this process. [4, 5] Therefore, the capacity of a battery is linked to how many Li ions the electrode can store. Many years have passed since the first commercialization of Li secondary battery in 1991, but Li cobalt oxide and graphite-based batteries are still being made without departing significantly from the conventional electrode materials. [6] In other words, a newly model of electric car can go farther because it has a large number of conventional batteries, not a new battery system. Various

attempts have been made to increase the capacity at the cathode and anode. Still, safety and stability concerns continue to prevent commercial implementation. [7–10] This paper presents the technology of surface engineering of Li metal anode for stable, high-capacity batteries.

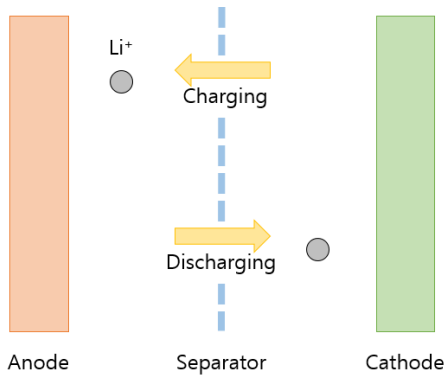

Figure 1.1 Main component of Li secondary battery

1.2 References

[1] M. Armand, Nature, 2001, 414, 359–367.

[2] M. Park, X. Zhang, M. Chung, G. B. Less and A. M. Sastry, J. Power Sources, 2010, 195, 7904–7929.

[3] M. Winter, B. Barnett and K. Xu, Chem. Rev., 2018, 118, 11433–11456.

[4] K. Xu, Chem. Rev., 2014, 114, 11503–11618.

[5] P. Arora and Z. Zhang, Chem. Rev., 2004, 104, 4419–4462.

[6] Y. Nishi, J. Power Sources, 2001, 100, 101–106.

[7] M. S. Whittingham, Chem. Rev., 2014, 114, 11414–11443.

[8] N. Yabuuchi, K. Kubota, M. Dahbi and S. Komaba, Chem. Rev., 2014, 114, 11636–11682.

[9] A. C. Luntz and B. D. McCloskey, Chem. Rev., 2014, 114, 11721–11750.

[10] M. N. Obrovac and V. L. Chevrier, Chem. Rev., 2014, 114, 11444–11502.

Chapter 2 Fundamental and literature review

2.1 Background on Li metal anode

It is necessary to use a high-capacity electrode material to make a high-capacity battery. Li metal is receiving the greatest attention as a potential anode material due to its superior theoretical capacity (3860 mAh g^{-1}), which is 10 times that of commercialized graphite anode. In addition, Li metal has low electrochemical potential (−3.04 V versus the standard hydrogen electrode) and is applicable to next-generation batteries such as Li-S and Li-air.

2.2 Issues with Li metal anode

When the anode is initially charged, the electrolyte is decomposed by a strong reducing atmosphere, and an SEI layer forms on the Li metal surface. [1] The SEI layer acts as a passivation layer that prevents further decomposition of the fresh electrolyte and at the same time acts as a conductor that transmits Li ions. [2,3] Widely used graphite anode has an intercalation–deintercalation mechanism in which Li ions intercalate between graphite galleries during charging. [4] That is, the graphite material can act as a host, so it does not undergo dramatic volume changes. However, Li metal is a hostless material that is charged and discharged by a plating-stripping mechanism. [5] Therefore, there is no space for Li ions to be charged

inside. As a result, upward expansion occurs when Li ion is plated. [3,5] Because the aforementioned SEI layer is brittle, it is broken by volume expansion during charging. At the same time, Li dendrites grow as the Li ion flux becomes focused on these cracks. (Figure 2.1) Li dendrites can penetrate the separator and contact the cathode. This process causes an internal short circuit, which creates a fire hazard due to Ohm's heat. During discharging, Li metal anode cannot maintain the expanded structure. Some of the Li metal remains uncharged, in a state away from the current collector, degrading the coulombic efficiency. If charging and discharging persists, the SEI layer is continuously broken and surface resistance accumulates, reducing the cycle stability of the battery. [5] Various studies have attempted to solve these problems. [6–11] Some studies have attempted to stabilize the surface using additives that decompose at a higher voltage range than the voltage of electrolyte decomposition, and other studies have attempted to suppress dendrite growth using solid-state electrolytes. [6,7] Yet other studies have attempted to secure the stability of the battery by applying protective layers on the Li metal surface. [8,9] Recently, attempts have been made to improve stability by adding Li fluoride to a Li metal protective layer. [10,11] After all, the main job of a protective layer is to keep the SEI layer stable when volume expansion of Li metal occurs. In order for the protective film to be more effective in the Li metal system, it must be manufactured with a thinner, lighter design. [12] The research to be introduced in this paper also moves the technology in a thinner, lighter direction while improving the stability of the Li metal battery.

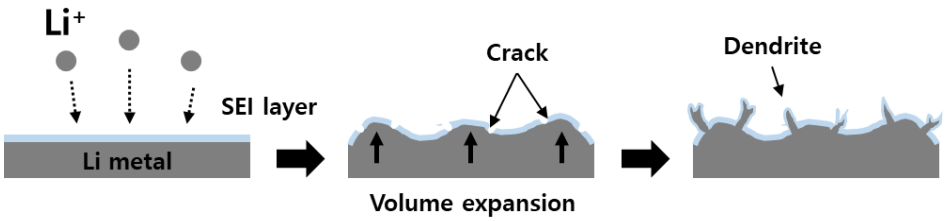

Figure 2.1 Mechanism of dendrite growth

2.3 References

[1] E. Peled and S. Menkin, J. Electrochem. Soc., 2017, 164, A1703–A1719.

[2] C. Han, Y. B. He, M. Liu, B. Li, Q. H. Yang, C. P. Wong and F. Kang, J. Mater. Chem. A, 2017, 5, 6368–6381.

[3] X. B. Cheng, R. Zhang, C. Z. Zhao and Q. Zhang, Chem. Rev., 2017, 117, 10403–10473.

[4] S. J. An, J. Li, C. Daniel, D. Mohanty, S. Nagpure and D. L. Wood, Carbon N. Y., 2016, 105, 52–76.

[5] D. Lin, Y. Liu and Y. Cui, Nat. Publ. Gr., 2017, 12, 194–206.

[6] X. Q. Zhang, X. B. Cheng, X. Chen, C. Yan and Q. Zhang, Adv. Funct. Mater., 2017, 27, 1–8.

[7] F. Zheng, M. Kotobuki, S. Song, M. O. Lai and L. Lu, J. Power Sources, 2018, 389, 198–213.

[8] Y. Liu, D. Lin, P. Y. Yuen, K. Liu, J. Xie, R. H. Dauskardt and Y. Cui, Adv. Mater., 2017, 29, 1–8.

[9] R. Xu, X. Q. Zhang, X. B. Cheng, H. J. Peng, C. Z. Zhao, C. Yan and J. Q. Huang, Adv. Funct. Mater., 2018, 28, 1–7.

[10] J. Lang, Y. Long, J. Qu, X. Luo, H. Wei, K. Huang, H. Zhang, L. Qi, Q. Zhang, Z. Li and H. Wu, Energy Storage Mater., 2019, 16, 85–90.

[11] D. Lin, Y. Liu, W. Chen, G. Zhou, K. Liu, B. Dunn and Y. Cui, Nano Lett., 2017, 17, 3731–3737.

[12] P. Albertus, S. Babinec, S. Litzelman and A. Newman, Nat. Energy, 2018, 3, 16–21.

Chapter 3 Three-dimensional mesh structure interlayer

3.1 Introduction

Lithium-ion batteries (LIBs) are widely used in various electronic systems such as electric vehicles, portable electronic devices, and mobile phones. As the demand for large-scale energy storage systems increases, a higher capacity battery is required. [1] In order to meet the demand for high capacity, it is essential to research higher capacity advanced active materials for cathode and anode. In cathode parts, Li excess layered oxide and Ni rich layered oxide have been investigated and some cases are commercialized. [2] In addition, various anode materials which have high theoretical capacity have been proposed to enhance energy density. [3-6] When Li ion battery is charged, Li cation is stored at the anode. When discharging, the charged capacity of the anode is used. It is important to study the anode part to provide stable high capacity. Most of high capacity anodic materials can be summarized of two type. The one is metal and metal oxide which have different lithiation mechanisms (alloying, conversion), and representative material is silicon and lithium. [7] The others are nano structured carbonaceous like CNT or graphene which physically stores energy by intercalation / deintercalation. [7,8] Among the anode materials, Li metal is an attractive electrode material with 4-10 times higher theoretical capacity (3860 mAh g^{-1}) and the lowest redox potential (−3.04 V vs. the standard hydrogen potential electrode). Also, Li metal is highly conductive

comparing silicon [1,2,9] and can be applied to Li ion batteries without any kind of additives such as conducive agent and binders. Furthermore, Li metal anode is essential to Li-air and Li-sulfur batteries, which are attracting attention as next-generation batteries. [9-11] However, the commercial graphite, whose theoretical specific capacity is only 372 mAh g^{-1}, is still used as dominant anode materials, because newly proposed anode materials can not satisfy commercial standard, especially cycling life. [6] Li metal anode have serious obstacles including moisture vulnerability and irregular Li growth. [12] Moisture vulnerability can be solved by controlling manufacturing condition. Meanwhile, Li dendrite growth issues are difficult to solve because these phenomena occurred during operating batteries. When Li ions are depositing on the Li metal, the electrolyte is reduced on the Li surface. This is called the solid electrolyte interphase (SEI) layer. [13] This layer acts as a passivation layer to pass Li ions while preventing other fresh electrolytes from decomposing with Li metal. However, because of the properties of a 'hostless' Li metal, while it continues to plate, the crack of Li metal surface will occur due to the infinite volume expansion, which makes it difficult to control the surface. [14] In this gap of crack, a new SEI layer is formed by meeting the fresh electrolyte and the ion flux enhanced by the cracks leads to a non-uniform Li plating. The Li dendrite formed under continuous cycling can grows and penetrate the separator. [15,16] It causes an internal short and safety problem. [17] When it starts stripping, the swollen volume returns to its original state and the SEI layer is broken without maintaining the formed structure. At this time, the Li metal surrounded by SEI layer is called dead Li, which causes a decrease in the coulombic efficiency. [18] During

cycling, the thick SEI layers and the dead Li accumulate on the Li metal and make safety hazard. [19] Because of these disadvantages of Li metal, it is difficult to apply to the anode of a next-generation battery. Li instabilities which is derived from the unstable SEI layer is an important challenge to be solved in Li metal batteries. In order to solve these problems, tremendous effort have been carried out to control the structure of the current collector to keep the SEI layer stable. The earlier approach is to form a stable SEI layer. In a classical manner, an electrolyte, such as $LiNO_3$, was added to build a stable SEI layer under initial charging and discharging conditions. [20] Artificial coating using Cu_3N and a styrene-butadiene rubber (SBR) composite were also studied. [21] The Cu_3N contact with the electrode turns into Li_3N, which is the fastest conductor that Li can penetrate. The volumetric expansion during charging and discharging is supported by the SBR. The other approach is to form a uniform pattern on the current collector where Li ions can be deposited uniformly or give space for volume expansion. When Li ions are deposited on a common current collector such as copper foil, Li nuclei was initially generated on current collector. And Li ion flux are concentrated in first nucleation sites which is called a hot spot, and this is major reason which leads to dendrite problems. [22] Therefore, it is possible to solve this problem by constructing a structure that can maintain the movement of Li ions homogenously. Also, by making voids, Li can keep the SEI layer from breaking during volume expansion. For this reason, 3D current collectors, such as a submicron skeleton or copper nanowire network, can effectively suppress the growth of dendrites. However, these processes must be added to create an artificial SEI layer, [23-26] and the 3D current collector is

actually placed under the Li metal in the battery system. Although the current collector has a 3D structure, it covered by the planar Li metal surface. Since the electrochemical reaction occurs on the surface of Li metal, it is difficult to use the structure of the current collector even if the structural stability is secured. In this study, a stainless steel mesh (SSM) is applied as an interlayer between Li metal and separator. SSM provide a relatively large surface area compared with the structure without interlayer, so that the specific current density is low and the Li ion can be uniformly plated on the SSM. Figure 3.1a displays the detail schematic representatives of the stripping-plating process. Planar Li have serious problems which cause safety issues. [21] During plating Li ions, planar Li foil does not maintain the SEI layer stably. [23,24] Because there is no space below, plated Li expands upward and pushing up the former layer. The SEI layer is broken to upward direction. Therefore, the Li ion flux is irregularly concentrated on these hot spots and grows into Li dendrite. [22] This grown Li dendrite penetrates the separator and reaches the cathode, eventually Li dendrite cause an internal short circuit and safety problems.

Additionally, when the stripping occurs, the structure that has been previously expanded cannot be maintained and destroyed. Unstable structure causes to accumulate dead Li that form an inactive layer, decrease coulombic efficiency. However, when SSM is applied, there is an empty space which is caused by mesh structure between Li metal and SEI layer, which extends downward and reduces the stress to the space below without breaking the SEI layer. Due to this structural advantage, the initially formed SEI layer stably remains. Also Li ion flux is

uniformly collected without formation of dendrite. Even though the inactive layer contains dead Li accumulates, it can prevent the decrease of the coulombic efficiency. Because it can transfer the electron through the SSM as matrix. Therefore, proposed SSM interlayer system that is applied between the Li metal and the separator is better than that of planar Li metal surface. Additionally, it is an economical and easy-to-apply strategy in which only SSM is added to the existing system.

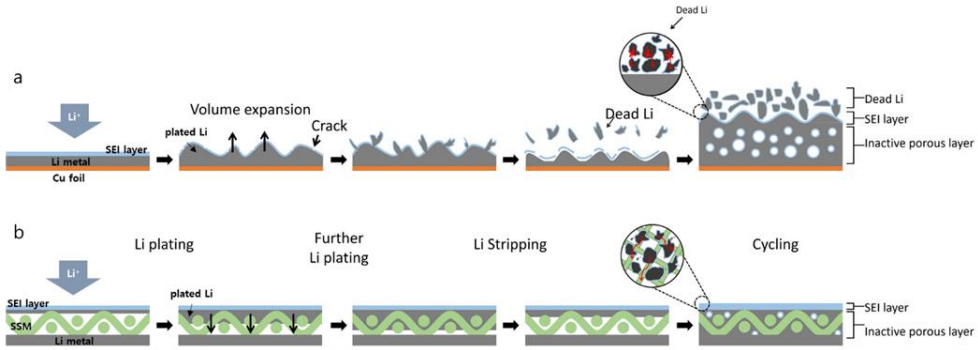

Figure 3.1 Schematic representatives of plating and stripping process of (a) conventional Li metal anode and (b) SSM applied Li metal anode.

3.2 Experimental section

3.2.1 Fabrication of stainless steel mesh interlayer

The surface was measured by Scanning Electron Microscopy (SEM). Figure 3.2 shows the picture of typical Li-metal foil, stainless steel mesh, and the prepared 3D SSM/Li composite electrode. Li metal is used as the anode and stainless steel mesh is used as the interlayer between anode and separator. The surface of a common Li metal is shown in the Figure 3.2a,d. On the surface of the Li metal, a certain pattern that generated during the making process was observed. The Figure 3.2b,e is the stainless steel mesh. It shows a pore size of 500 μm. (The diameter is 15 mm and the thickness is 0.15 mm.) When the SSM is pressed on the Li metal surface, it is pressed into the SSM matrix by the ductility of the Li metal. (Figure 3.2c) However, it can be seen that the Li metal doesn't penetrate into the SSM matrix in the Figure 3.2f. Because of using the structure as an interlayer, SSM/Li electrode isn't applied with high pressure. Planar Cu used as a current collector in Half-cell test is shown in Figure 3.3. Figure 3.2g shows the SSM applied electrode structure. Since the electrochemical reaction takes place on the surface of Li metal, applying an interlayer to the metal surface can ensure stability effectively even with Li metal foil.

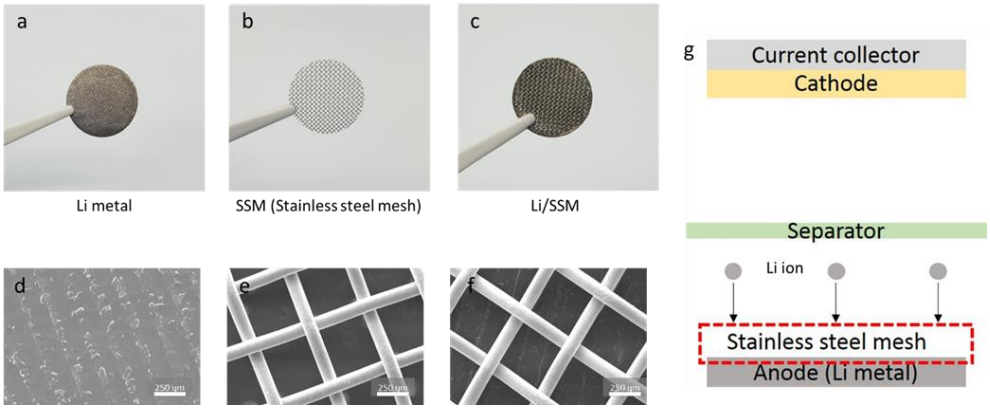

Figure 3.2 Surface pictures of (a) Li metal, (b) SSM, and (c) Li/SSM (Li on SSM). SEM images of (d) Li metal, (e) SSM, and (f) Li/SSM. (g) Schematic of the interlayer position of the Li metal battery.

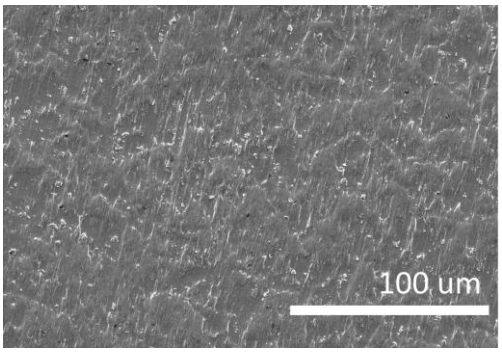

Figure 3.3 SEM image of Cu foil

3.2.2 Characterization of stainless steel mesh interlayer

Stainless steel used in the experiment was used 304 Stainless Steel Meshed Disc, and the detailed characteristics are shown in Table 3.1

Material	Stainless Steel. Purity > 99.9 %
Diameter	15 mm
Thickness	0.15 mm

Stainless Steel	C	Si	Mn	P	S	Ni	Cr
SUS 304	0.08	1.00	2.00	0.045	0.03	8.00~10.50	18.00~20.00

Table 3.1 Properties of stainless steel mesh

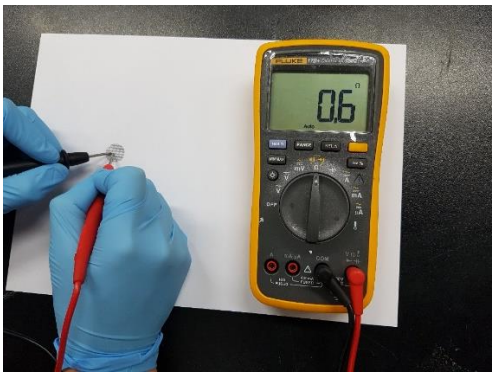

Figure 3.4 Resistance of stainless steel mesh

3.2.3 Surface analysis and electrochemical measurement

Galvanostatic cycling measurements in the half-cell structure were measured with a 3 electrode system to analyze the behavior of plated/stripped Li ions on the surface. The structural stability of the SEI layer can be confirmed through galvanostatic cycling measurements. Planar Cu and the SSM were used as the working electrodes, and Li metal foil was used as the counter and reference electrodes. Before the test, the cells were first cycled at 0–1 V (vs. Li^+/Li) at 50 μA for five cycles for initialization, to remove surface contaminations and stabilize the interface (Figure 3.5). [22] Li ions were plated on the current collector at 1 mA cm^{-2} and stripped up to 1 V (Figure 3.6a). Figure 3.6b demonstrates Nyquist plots of the prepared half-cells. The SSM was added to the interlayer, but it had a negligible effect on the overall resistance. During the plating process, the Li ions are plated on the surface of the working electrode (E_{wk}) as simulated in Figure 3.7a and some Li ions are used to form the SEI layer (Figure 3.7b) due to the strong reducing condition of the surface of E_{wk}. Li ions deposited on the surface of the opposite electrode (E_{ct}/E_{ref}) are stripped during discharging. However, Li ions used for formation of the SEI layer remain as an inactive layer (Figure 3.7). [27] Therefore, the ratio of the plated Li ions and the stripped Li ions is different. This ratio is called coulombic efficiency. [26] Even if the cycle is continued, the stable SEI layer maintains a constant coulombic efficiency because there is no more use of Li ions for additional SEI layer formation. Thus, the more stable structure allows the SEI layer to remain unbroken. Figure 3.6c shows the coulombic efficiency results of planar Cu and SSM.

Planar Cu did not show constant coulombic efficiency. The coulombic efficiency begins to decrease gradually and decreases sharply after 31 cycles. At last, planar Cu cannot exceed 50 cycles and cell failure occurs. The loss of coulombic efficiency with planar Cu indicates the formation of dead Li which is related to continuous SEI layer formation and destruction due to unstable volume changes of the SEI layer deposited planar Cu structure. In contrast, the SSM remained constant over the cycles and showed 98.35% coulombic efficiency after 50 cycles. This indicates that the SSM structure prevents the SEI layer from being cracked and suppresses Li ions from forming an inactive layer during volume expansion and contraction. We also compared SSM with planar stainless steel to check whether the result is due to the material properties, and not the structural difference between Cu and the SSM. Planar stainless steel shows an unstable behavior after 30 cycles, followed by cell failure like that which occurred with the planar Cu structure. Therefore, these results demonstrate that the SSM is a more stable structure than the planar structures.

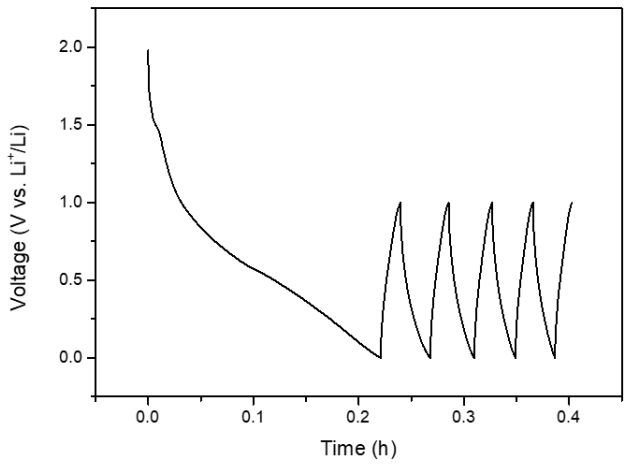

Figure 3.5 The voltage profile of half-cell test during initialization process. The batteries were first cycled at 0–1 V (vs. Li^+/Li) at 50 μA for five cycles for initialization to remove surface contaminations and stabilize the interface.

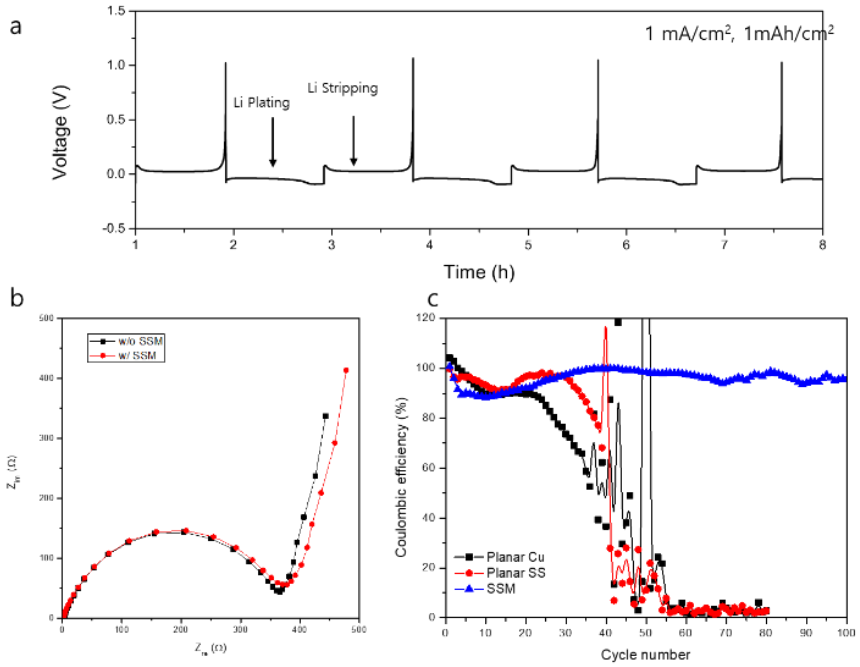

Figure 3.6 (a) The voltage profile of the plating and stripping process at 1 mA cm^{-2}, (b) Nyquist plot of half-cell tests with planar Cu (black) and SSM (red) and (c) coulombic efficiency of half-cell tests with planar Cu (black), planar SSM (red), and SSM (blue).

$$Coulombic\ efficiency = \frac{Charge\ of\ stripped\ Li\ ion}{Charge\ of\ plated\ Li\ ion}$$

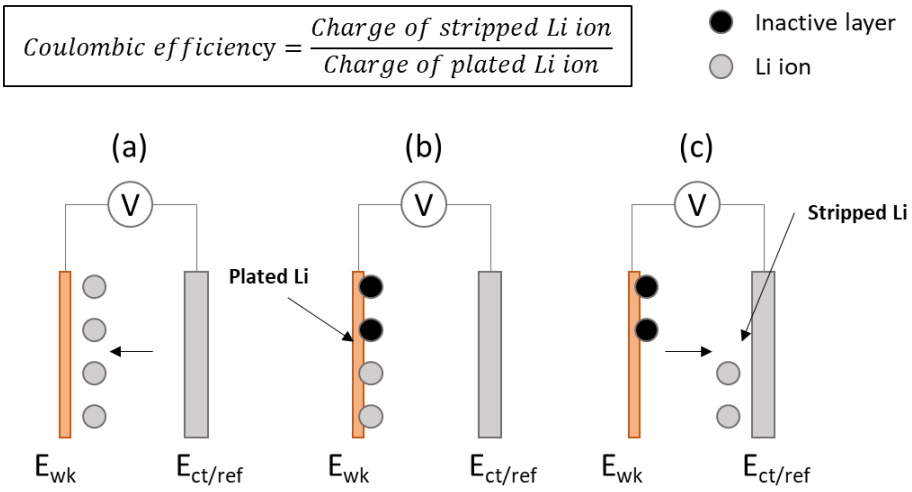

Figure 3.7 Schematic illustrations of half-cell tests.

Figure 3.8 shows SEM images of the working electrode surface after 0, 50, and 100 cycles, respectively. The surface image was captured after stripping. The layer deposited on the surface is an inactive layer. In unstable structures, cracks are formed due to uneven Li^+ deposition and volume expansion. [20] As shown in Figure 3.8a and b, cracks are observed in the inactive layer on the planar Cu surface after 50 cycles. When the Li dendrites are formed due to the Li ion flux being concentrated in these cracks, cell failure occurs. Figure 3.8c after 100 cycles shows cracks and a non-uniform surface, because the uneven surface makes the Li flux more nonhomogeneous and the inactive layer accumulates continuously. Figure 3.8d and e indicate a uniform surface. It can be confirmed that the inactive layer formed on the surface stably and was maintained in the original matrix structure after 50 cycles. Unlike planar Cu, the Li ion flux was homogeneously plated and all surfaces were smooth surfaces without cracks. As shown in Figure 3.8, the SSM can be seen to have a smooth surface even after 100 cycles. The SSM has many voids with conductive properties. So, when the SSM is in contact with the lithium anode surface as a protective layer, the local charge density maintains a uniformly spread state from the lithium anode to the SSM. Therefore, the SEI layer firstly formed on the top of the SSM, not the surface of the Li metal anode. When plating, the Li cations transferred into the SSM voids (pore) through the SEI layer. So as shown in the SEM images (Figure 3.8h and i), the Li cations are accumulated preferentially in the direction of filling the voids in our structure. As a result, the SSM structure keeps the structure stable in the volume expansion of the Li metal better than in that of planar Cu.

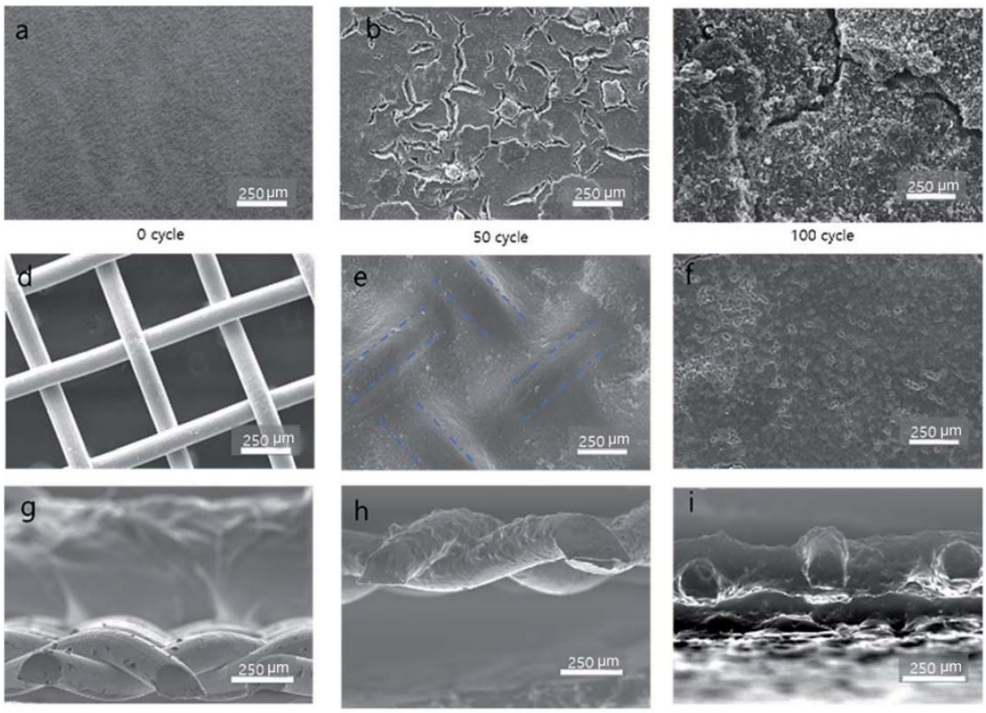

Figure 3.8 SEM images of the surface of Li deposited on Cu foil and the SSM with a current density of 1 mA cm^{-2}. SEM images of the surface of pristine Cu foil and the SSM applied Cu foil (a), (d) and (g) after 50 cycles (b), (e) and (h) and after 100 cycles (c), (f) and (i).

The result is shown in Figure 3.9a with current densities of 1 mA cm^{-2}. When Li metal without the SSM interlayer is used, it exhibits unstable behaviour in the initial cycles, and the voltage at 10 hours is 0.113 V, which increases steadily up to 0.827 V by 165 hours. This is because, as described above, the inactive layer continues to accumulate on the surface, which increases the surface resistance. After 165 hours, the oscillation occurs in the high voltage range between 23.1 mV and 1.10 V. This is due to the following reasons. The inactive layer, which has formed thickly, is broken by the volume expansion, and the surface resistance instantaneously decreases and the voltage is dropped. When the crack is covered by plating, the voltage rises again to the high voltage range. On the contrary, when the SSM is used as an interlayer on Li metal, it shows very stable behaviour even after 250 hours. When adopting the SSM interlayer, voltage increments are nearly negligible compared to Li metal without the SSM interlayer. The voltage peak of the SSM is 43 times smaller than that of Li metal at 25 hours. Of course, inactive layers are formed on the SSM interlayer. A millivolt scale graph profile applied to the SSM interlayer showed that the voltage increases in small scale units. However, the SSM interlayer showed much better cycle behaviour than that of bare Li metal, due to the excellent stability of the SSM layers caused by their own structure. The graph for the applied current density of 5 mA cm^{-2} is shown in Figure 3.9b. In general, the use of planar Li metal has limited its ability to maintain stability at the actual operating conditions of 5 to 10 mA cm^{-2}. [27] Compared to 1 mA cm^{-2}, the planar metal with 5 mA cm^{-2} oscillates from the initial cycles to a larger voltage range up to 0.888 V, and continues to exhibit unstable behaviour without a period of increased

resistance that the inactive layer partially retains. However, the structure using the SSM interlayer shows very stable behaviour with a large current density of 5 mA cm^{-2}. Over time, as the inactive layer is accumulated, the voltage rises 16.6 mV at a small scale without a period of soaring voltage. As shown in Figure 3.10 after 200 hours, the SSM applied cells have a rectangular shape with constant plating and stripping potential. However, when using only Li metal, the plating stripping potential is high and unstable. The SSM matrix leads to a uniform charge distribution with a high surface area, and can effectively control the volume change. Therefore, without changing the Li metal to a 3D structure, the planar Li metal can be used by only applying the interlayer.

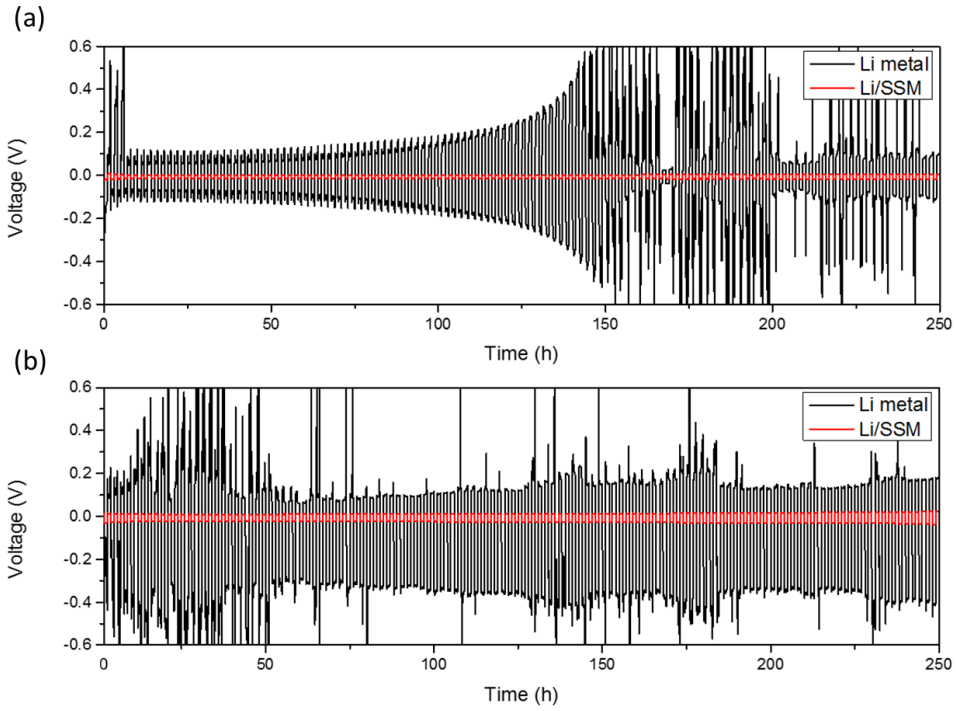

Figure 3.9 Symmetrical cell tests. (a) The voltage profile with the bare Li metal (black) and Li/SSM (red) electrode for 250 hours at 1 mA cm^{-2} and (b) the voltage profile with the bare Li metal (black) and Li/SSM (red) electrode for 250 hours at 5 mA cm^{-2}.

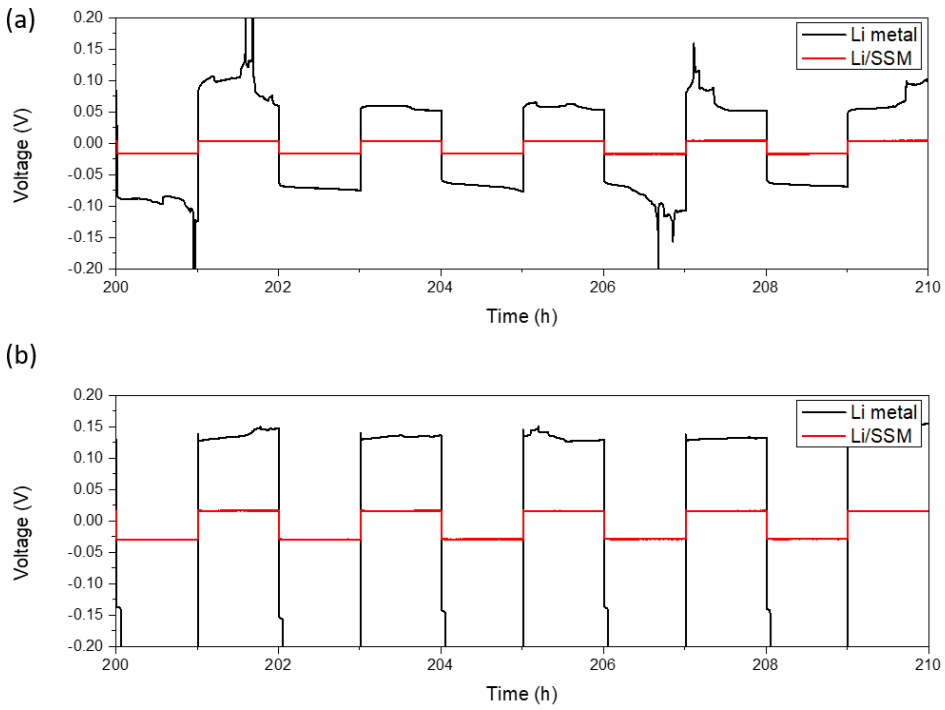

Figure 3.10 Symmetrical cell tests. (a) The voltage profile with the bare Li metal(black) and Li/SSM(red) electrode between 200 hours and 210 hours at 1 mA cm^{-2} (b) The voltage profile with the bare Li metal(black) and Li/SSM(red) electrode between 200 hours and 210 hours at 5 mA cm^{-2}

In Figure 3.11, voltage hysteresis is the average of the difference in voltage between plating and stripping of each cycle, and is shown below equation.

$$\text{Voltage hysteresis} = \frac{V_{Max_{stripping}} - V_{min_{plating}}}{2}$$

At 1 mA cm^{-2}, Li metal accumulates the inactive layer and increases its resistance, so the voltage rises to 0.962 V. After 90 cycles, the surface breaks and the voltage oscillates. However, when the SSM is applied as an interlayer, a stable profile can be confirmed, and the voltage range is between 8 mV and 16 mV. When 5 mA cm^{-2} is applied, Li metal does not maintain a stable surface from the beginning and voltage surges up to 0.967 V. But, as in the case of 1 mA cm^{-2}, it can be confirmed that the SSM keeps the surface stable. The voltage range is between 16 mV and 44 mV when comparing the SSM at 1 mA cm^{-2} and 5 mA cm^{-2} in Figure 3.11, and the higher the current density applied, the more the inactive layer tends to accumulate, and this inactive layer increases the resistance. Nevertheless, the voltage does not seem to oscillate rapidly such as with Li foil. Since the electrochemical reaction takes place on the surface of Li metal, applying an interlayer to the metal surface can ensure stability effectively, even with Li metal foil. Figure 3.12 shows the hysteresis of three SSMs with different hole sizes (50 mesh, 100 mesh, 300 mesh). As mentioned, the hysteresis of the Li metal anode without the SSM was about 1 V, while the SSM applied Li metal anode showed stable behaviour of less than 15 mV. In addition, a similar value was shown without any special tendency to depend on

the mesh size, so the 3D conductivity structure had a greater impact on maintaining a stable Li metal anode than the pore size of the mesh did.

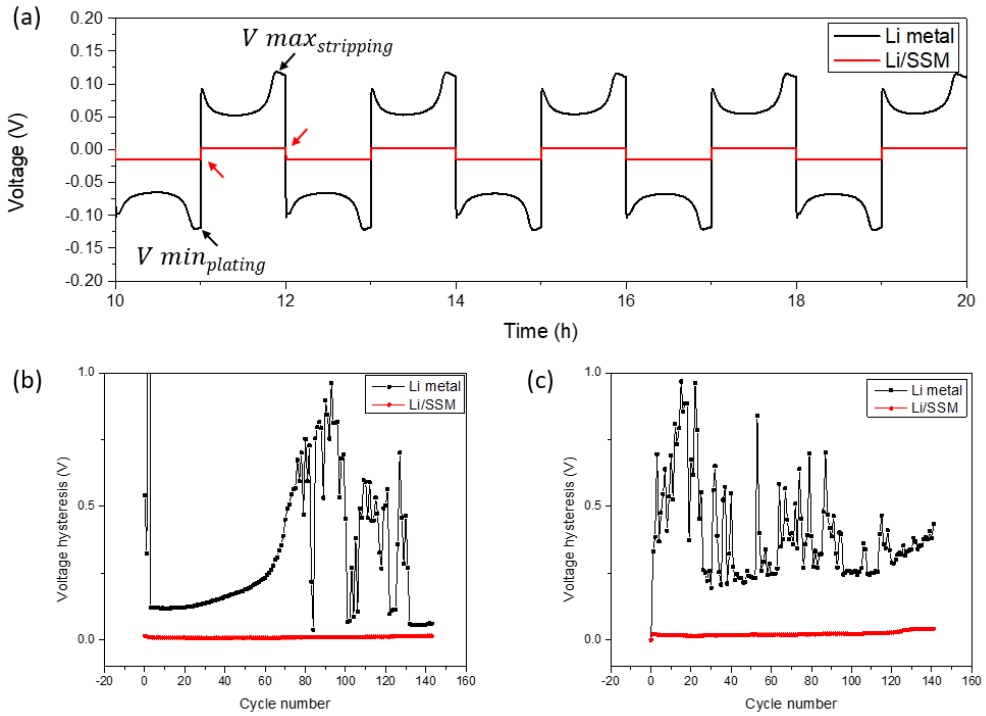

Figure 3.11 (a) The voltage profile of Li plating/stripping in symmetrical cells, (b) the voltage hysteresis at 1 mA cm^{-2} and (c) the voltage hysteresis at 5 mA cm^{-2}

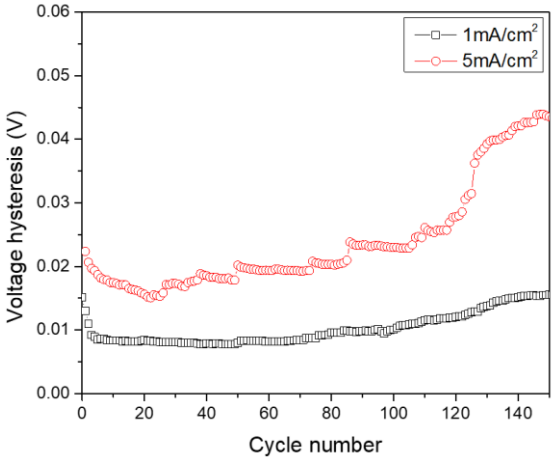

Figure 3.12 The voltage hysteresis in symmetric Li/SSM cells

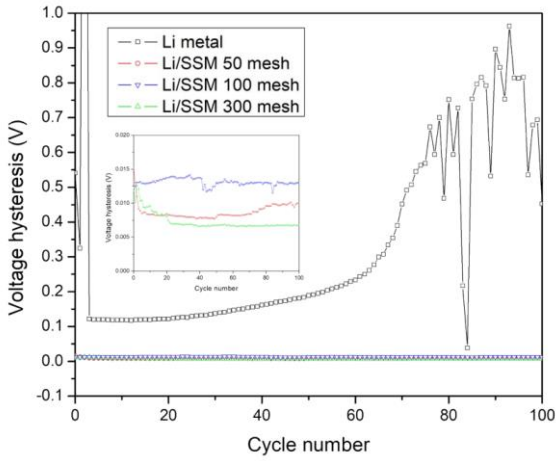

Figure 3.13 The voltage hysteresis at 1mA cm^{-2} with different mesh size

3.2.4 Effect of stainless steel mesh interlayer for Li metal battery

Galvanostatic cycling tests with Li/$LiFePO_4$ were conducted to confirm whether the interlayer was effective in real battery systems (Figure 3.14a). [28] The coulombic efficiency of the cells without the SSM dropped to 58.71% (Figure 3.14b), however that of the cells with SSM remained at 65.73% (Figure 3.14c). As a result, we confirmed that the capacity reduction of cells with the SSM was more reliable at high cycling rate than cells that the SSM was not applied to.

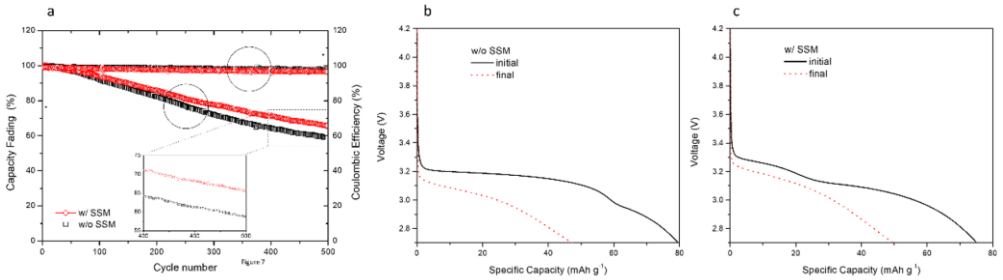

Figure 3.14 (a) The capacity fading profile (b), (c) The initial and final discharging capacity profile

3.3 Conclusion

As a result, we have reported a simple and inexpensive strategy to apply an SSM interlayer to keep a Li metal battery stable when Li is plated/stripped from the surface. The SSM structure solves the problem of instability in Li metal, because the hostless Li metal maintains the stable SEI layer by providing a matrix for infinite volume expansion and keeps the Li ion homogeneous on the surface. The large surface area can also solve the decrease of coulombic efficiency due to dead Li. The SSM structure maintains a coulombic efficiency of 98.35% and a stable profile is retained even after 250 hours at 1 mA cm^{-2}. Also, a large current density (5 mA cm^{-2}) which was not applicable to planar Li could be applied only by adopting the SSM interlayer. In the half cell test using $LiFePO_4$/Li, the capacity faded to a 58.71% level compared to the initial capacity when the SSM was not applied under the conditions of 5C, otherwise the cell where the SSM was applied was maintained at 65.73%. As a result, this SSM structure will be an effective method to secure stability simply by applying a Li anode used in large capacity batteries such as Li–S and Li–air.

3.4 Experimental details

Fabrication of SSM interlayer/Li metal composite anode

Li metal foil was first cut with a circle-shaped cutter with a diameter of 15 mm. Stainless steel mesh with a diameter of 15 mm and 50 mesh was also purchased from MTI Korea. 50 is the number of holes in the area of 1 square inch. The stainless steel mesh was aligned with the circular Li metal foil and pressed with a punching machine until the stainless steel mesh was slightly embedded in the surface of Li metal.

Electrochemical measurements

CR2032 coin cells were assembled to evaluate the coulombic efficiency, surface stability, and galvanostatic charging/discharging. All manufacturing processes were performed in an argon-filled glove box. The galvanostatic cycling measurements in half-cells were performed with a current density of 1 mA cm^{-2}. The planar Cu, planar stainless steel, and stainless steel mesh were used as the working electrodes, and Li metal foil was used as the counter and reference electrodes. The separator of polypropylene (25 μm) and electrolyte of 1 M $LiPF_6$ in EC (ethylene carbonate)/DEC (diethyl carbonate) (50/50 by volume, 50 μL) were obtained from Celgard and PANAX ETEC Co. Ltd, respectively. Cycle tests were performed using WBCS3000 (WonATech Co.) Before the test, the cells were first cycled at 0–1 V (vs. Li^+/Li) at 50 μA for five cycles. 1 mA h cm^{-2} of Li was plated on the current

collector at a current density of 1 mA cm^{-2}, followed by Li stripping up to 1 V. The galvanostatic cycling measurements in the symmetrical cell test were performed at current densities of 1 mA cm^{-2} and 5 mA cm^{-2}. The Li metal foil was purchased from MTI Korea and used as the working electrode, and Li metal foil was used as the counter and reference electrode. The separator and electrolyte were the same as in the half-cell tests. Stainless steel mesh was used as the interlayer between the Li metal foil and the separator. The cells were charged and discharged at 1 mA cm−2 for 1 h and 5 mA cm^{-2} for 1 h in each symmetrical cell (charging/discharging = 1 h/1 h). $LiFePO_4$ was used as the cathodic material for the Li metal battery. $LiFePO_4$ was applied as a slurry type with a bar coating method (cathode slurry composition: $LiFePO_4$ (MIT Korea) : Super P (Timcal) : polyvinylidene fluoride (Kynar) = 8 : 1 : 1 w/w/w). The Li metal battery was charged and discharged under the conditions of 5C for 500 cycles.

Scanning electron microscope analysis

Scanning electron microscope (SNE-4500M, SEC) analysis was conducted on a field emission scanning electron microscope at 15 kV. After electrochemical tests, the cells were carefully disassembled in an Ar-filled glove-box. Then Li–metal anodes were rinsed with DEC three times to remove the residual electrolytes, and subsequently dried under vacuum at room temperature for 24 h.

3.5 References

[1] B. Dunn, H. Kamath, J.-M. Tarascon, Science, 2011, 334, 928-935.

[2] P. Rozier, J. M. Tarascon, J. Electrochem. Soc., 2015, 162, A2490-A2499.

[3] C. K. Chan, H. Peng, G. Liu, K. McIlwrath, X. F. Zhang, R. a Huggins, Y. Cui, Nat. Nanotechnol., 2008, 3, 31-35.

[4] H. Kim, J. Cho, Nano Lett., 2008, 8, 3688-3691.

[5] B. Sun, Z. Chen, H. S. Kim, H. Ahn, G. Wang, J. Power Sources, 2011, 196, 3346-3349.

[6] J. M. Tarascon, M. Armand, Nature, 2001, 414, 359-367.

[7] S. Goriparti, E. Miele, F. De Angelis, E. Di Fabrizio, R. Proietti Zaccaria, C. Capiglia, J. Power Sources, 2014, 257, 421-443.

[8] W. Yuan, Y. Zhang, L. Cheng, H. Wu, L. Zheng, D. Zhao, J. Mater. Chem. A, 2016, 4, 8932-8951.

[9] D. Lin, Y. Liu, Y. Cui, Nat. Nanotechnol., 2017, 12, 194-206.

[10] L. Li , C. Liu , G. He , D. Fan and A. Manthiram , Energy Environ. Sci., 2015, 8 , 3274.

[11] L. Li , T. A. Pascal , J. G. Connell , F. Y. Fan , S. M. Meckler , L. Ma , Y.-M. Chiang , D. Prendergast and B. A. Helms , *Nat. Commun.*, 2017, **8** , 2277.

[12] X. B. Cheng, R. Zhang, C. Z. Zhao, F. Wei, J. G. Zhang, Q. Zhang, Adv. Sci., 2015, 3, 1-20.

[13] E. Peled, S. Menkin, J. Electrochem. Soc., 2017, 164, A1703-A1719.

[14] S. Sen Chi, Y. Liu, W. L. Song, L. Z. Fan, Q. Zhang, Adv. Funct. Mater., 2017, 27, 1-10.

[15] H. Wu, D. Zhuo, D. Kong, Y. Cui, Nat. Commun., 2014, 5, 1-6.

[16] M. H. Ryou, D. J. Lee, J. N. Lee, Y. M. Lee, J. K. Park, J. W. Choi, Adv. Energy Mater., 2012, 2, 645-650.

[17] Y. Ahn, J. Park, D. Shin, S. Cho, S. Y. Park, H. Kim, Y. Piao, J. Yoo, Y. S. Kim, J. Mater. Chem. A, 2015, 3, 10715-10719.

[18] R. Bhattacharyya, B. Key, H. Chen, A. S. Best, A. F. Hollenkamp, C. P. Grey, Nat. Mater., 2010, 9, 504-510.

[19] W. S. Kim, W. Y. Yoon, Electrochim. Acta, 2004, 50, 541-545.

[20] Ding, L. Zhou, C. Zhou, D. Geng, J. Yang, S. W. Chien, Z. Liu, M.-F. Ng, A. Yu, T. S. A. Hor, M. B. Sullivan, Y. Zong, Sci. Rep., 2016, 6, 33154.

[21] Y. Liu, D. Lin, P. Y. Yuen, K. Liu, J. Xie, R. H. Dauskardt, Y. Cui, Adv. Mater., 2017, 29, 1-8.

[22] W. Liu, D. Lin, A. Pei, Y. Cui, J. Am. Chem. Soc., 2016, 138, 15443-15450.

[23] Q. Li, S. Zhu, Y. Lu, Adv. Funct. Mater., 2017, 27, 1606422.

[24] C.-P. Yang, Y.-X. Yin, S.-F. Zhang, N.-W. Li, Y.-G. Guo, Nat. Commun. 2015, 6, 8058.

[25] Q. Yun, Y. B. He, W. Lv, Y. Zhao, B. Li, F. Kang, Q. H. Yang, Adv. Mater., 2016, 6932-6939.

[26] L. L. Lu, J. Ge, J. N. Yang, S. M. Chen, H. Bin Yao, F. Zhou, S. H. Yu, Nano Lett., 2016, 16, 4431-4437.

[27] L. Gireaud, S. Grugeon, S. Laruelle, B. Yrieix, J. M. Tarascon, Electrochem. commun., 2006, 8, 1639-6939.

[28] K. S. Ng, C. S. Moo, Y. P. Chen, Y. C. Hsieh, Appl. Energy, 2009, 86, 1506-1511.

[29] D. Lin, J. Zhao, J. Sun, H. Yao, Y. Liu, K. Yan, Y. Cui, Proc. Natl. Acad. Sci. 2017, 114, 4613-4618.

Chapter 4 Thermal crosslinked polymer protective layer

4.1 Introduction

Owing to their limited theoretical capacity, commercial Li-ion batteries are incapable of satisfying the high-energy-density requirement resulting from the increasing demand for electric vehicles, energy storage systems, and portable electronics. [1-3] Li metal is considered the most promising anode material in rechargeable Li batteries because of its highest theoretical capacity (3860 mAh g^{-1}), which is 10 times the theoretical capacity of the conventional graphite anode (372 mA h g^{-1}), low density (0.59 g cm^{-3}), and the lowest redox potential (−3.04 V versus the standard hydrogen electrode). [4-6] However, its infinite volume expansion through a mechanism that is not a host-guest mechanism but a plating-stripping mechanism causes major problems (Figure 4.1a). [4-6] Owing to the highly reactive environment of the anode, the organic solvent decomposes on the anode surface during the initial charging process and instantly forms a solid electrolyte interphase (SEI) layer, which is a passivation layer. [7,8] This layer serves not only as an ionic conductor, allowing Li ions to pass through, but also as an electronic insulator, preventing the further decomposition of the electrolyte during the charging-discharging process. [6] However, Li metal cannot maintain the initial SEI layer

owing to its volume expansion, and gaps are formed in the SEI layer. These gaps reduce the surface resistance and become locations with high concentrations of Li ions, leading to dendrite formation. If this dendrite grows, it penetrates the separator and comes in contact with the cathode, causing internal short circuits. [9] Therefore, dendrite growth is a safety hazard. During the discharge process, which is accompanied by volume contraction, dendrites break away from the Li metal surface and become “dead Li”. [4] The dead Li lowers the coulombic efficiency and the dead Li accumulated on the anode surface acts as a resistance component, degrading the battery performance during the cycling process. To solve this problem, many studies have investigated ways to stabilize the surface of Li metal. [9-12] In particular, many attempts have been made to improve the cycling stability of Li metal batteries by coating polymer materials on the surface of the Li metal. [13-17] In this chapter, we present a simple and green method to stabilize the surface of Li metal. The method involves the thermal cross-linking of poly(ethylene glycol) dimethacrylate (PEGDMA) containing ethylene oxide units capable of transferring Li ions to Li metal and mechanical strength. [18-20] A cross-linked PEGDMA (c-PEGDMA) protective film was fabricated on a Li metal surface using a bar coater, and it was thermally cured for 1 min at 100 ℃. A schematic of the c-PEGDMA layer is presented in Figure 4.1b. The c-PEGDMA on the surface of Li metal acts as a solid electrolyte as well as a polymer matrix that inhibits the volume expansion of and dendrite growth on the Li metal (Figure 4.1c). It can be used efficiently at the electrode surface. Surface analysis and electrochemical experiments were conducted to confirm the effect of the c-PEGDMA protective layer.

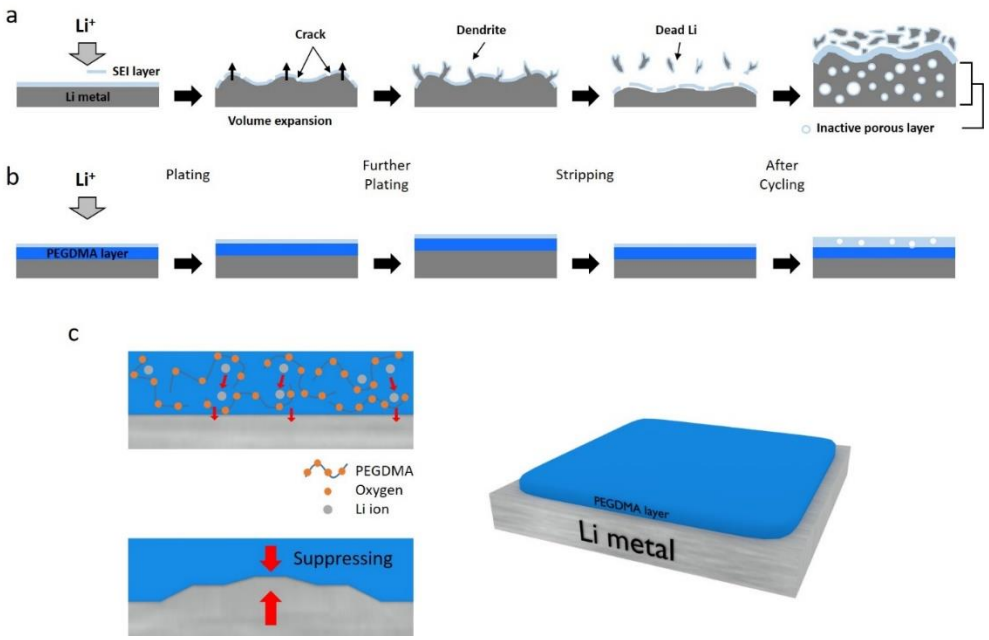

Figure 4.1 Schematic illustrations of the plating and stripping behavior of (a) a conventional bare Li metal anode and (b) PEGDMA protective layer applied Li metal anode. (c) Schematic illustrations of effect of PEGDMA protective layer.

4.2 Experimental section

4.2.1 Fabrication of PEGDMA protective layer

0.01 g of tert-Butyl peroxypivalate was added into 1 g of poly (ethylene glycol) dimethacrylate. This solution was stirring at room temperature and dropped onto lithium metal surface. This droplet coated with the bar coater to make a film on the lithium metal surface. After casting process, polymerization of Poly (ethylene glycol) dimethacrylate was obtained for 1 minute with 100 ℃ on hot plate. Manufacturing processes of PEGDMA protective layer were performed in an argon-filled glove box.

4.2.2 Characterization of PEGDMA protective layer

The prepared c-PEGDMA was analyzed using attenuated total reflection infrared spectroscopy in the range of 3500–700 cm^{-1} as described Figure 4.3a. The absorption peaks located at 946.4–749.3 cm^{-1} indicate the C–H deformation vibration and in-plane C–C in PEGDMA and c-PEGDMA. [21] Peaks at 1636.1–1638.2 cm^{-1} and 1716.2–1724.4 cm^{-1} denote C[double bond, length as m-dash]C stretching and C[double bond, length as m-dash]O stretching in the acrylate group, respectively. The peak intensity of C[double bond, length as m-dash]C apparently decreased after the cross-liking reaction. The conversion ratio, which is derived

from the cross-linking reaction, was calculated as the ratio of C[double bond, length as m-dash]C to C[double bond, length as m-dash]O, since cross-linking involved the conversion of C[double bond, length as m-dash]C bonds to C–C bonds. The transformation of PEGDMA into c-PEGDMA occurred at a conversion ratio of 27.97%. The low value implies that the cross-linking rate of c-PEGDMA was low, which in turn indicates that the mobility of c-PEGDMA was appropriate for conducting Li ions. As this reason, we can obtain flexible and ion conductive cross-linked polymer protective layer. Other peaks that were obtained are listed in Table 4.1 Electrochemical impedance spectroscopy was performed to confirm the interfacial resistance (Figure 4.3b). The bulk resistance (R_{Ω}) of the c-PEGDMA-coated Li metal was similar to that of the uncoated Li metal (2–3 Ω) since c-PEGDMA was ion conductive and the same electrolyte was used. The conductivity of liquid electrolyte was 6.9 mS cm^{-1} and liquid electrolyte wit c-PEGDMA protective film was 6.6 mS cm^{-1}. Based on these results, the PEGDMA protective layer has a level of ion conductivity that does not interfere with the conductivity of Li ions (Figure 4.3). Furthermore, the charge transfer resistances of the two Li metals were almost identical. Thus, the interfacial resistance of the c-PEGDMA coating was negligible. The c-PEGDMA film had characteristics such as high transparency, softness, and flexibility (Figure 4.2c). The c-PEGDMA protective film had a tensile strength of 4.94 MPa (Figure 4.4). In a swelling test for electrolyte, the original volume of the cross-linked c-PEGDMA was maintained after one week (Figure 4.5).

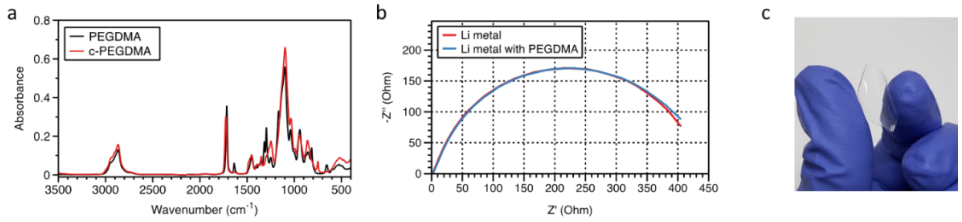

Figure 4.2 (a) Attenuated total reflection infrared spectroscopy of PEGDMA and c-PEGDMA (b) Nyquist plot of Li metal (red) and Li metal with PEGDMA (blue). (c) Image of fabricated PEGDMA film. SEM images of the surface of Li metal with a current density of 1 mA cm^{-2}

Functional group	Peaks [cm^{-1}]
C-O stretching of ethylene oxide	1242~1250
C-H bending of alkane	1421~1454
C=C stretching of alkene	1636~1639
C=O stretching of conjugated aldehyde	1716~1724
C-H stretching of aldehyde	2867~2869
C-H stretching of alkane	2939~2945

Table 4.2 Absorption peaks table of ATR FT-IR of c-PEGDMA.

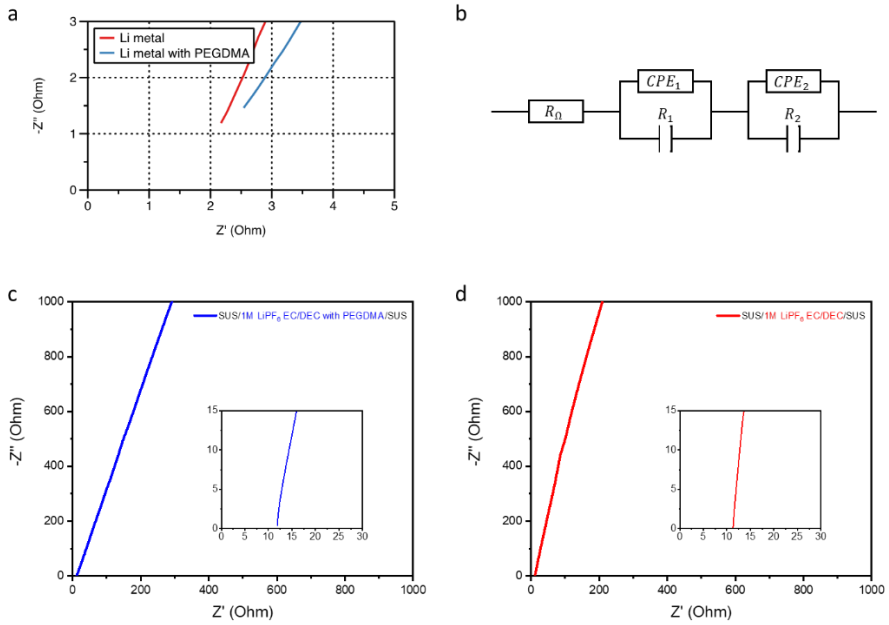

Figure 4.3 (a) Nyquist plot of Li metal (red) and Li metal with PEGDMA (blue), (b) Equilibrium circuit of Li symmetrical cell, (c) Nyquist plot of 1M $LiPF_6$ in EC/DEC with PEGDMA using stainless steel (SUS), (d) Nyquist plot of 1M $LiPF_6$ in EC/DEC using stainless steel.

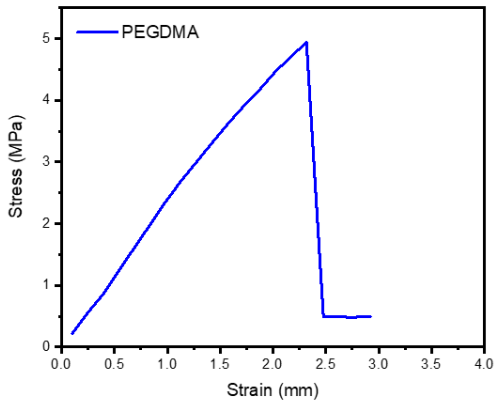

Figure 4.4 The mechanical property of c-PEGDMA film

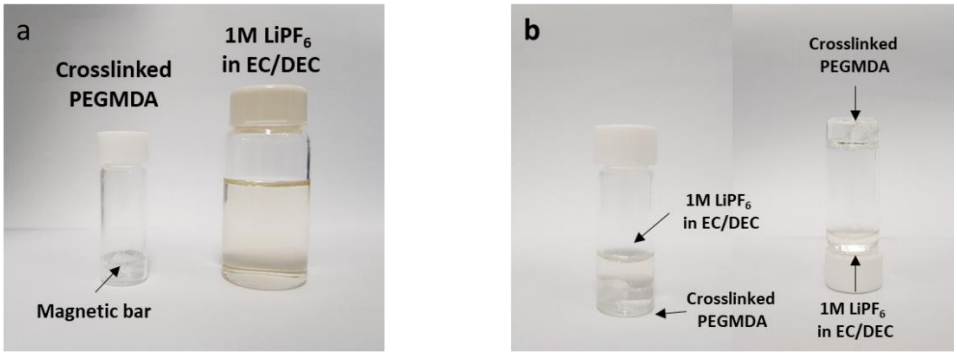

Figure 4.5 (a) Images of crosslinked PEGDMA and 1M $LiPF_6$ in EC/DEC (b) Images of mixed with crosslinked PEGDMA and 1M $LiPF_6$ in EC/DEC after 7 days.

4.2.3 Surface analysis and electrochemical measurement

Scanning electron microscopy (SEM) was performed for investigating the surfaces of coated and uncoated Li metals. The measurement result for a pristine Li metal is shown in Figure 4.6a. The Li metal shows a horizontal stripe pattern created by a roll-to-roll process and its thickness is 230 μm (Figure 4.6b). In cycle experiments, no additives were used, since only the effect of the surface protective film was to be confirmed. The result of the cycle experiment for a bare Li metal after 100 charge–discharge cycles is shown in Figure 4.6c. It shows accumulated inactive layer caused by process that SEI layer is broken by the volume expansion of Li metal and the electrolyte is decomposed again to recover it. Figure 4.6d shows that the thickness of the Li metal is 331.5 μm, which is greater than the thickness of the bare Li metal by 101.5 μm. [22] This result of cross-section reveals a large number of dendrites growing upward. The surface coated with c-PEGDMA is shown in Figure 4.6e. The coating covering the Li metal surface has a wrinkled morphology which was naturally formed during cross-linking. Owing to the coating, it is difficult to observe the horizontal stripe pattern observed on the surface of the bare Li metal. Figure 4.6f shows the same cross section that was earlier shown for the bare Li metal, and it is covered with 8.0 μm thick c-PEGDMA. If the crosslinked PEGDMA does not contain a liquid electrolyte, the protective layer is considered to be similar to the solid polymer electrolyte based on segmental motion. Therefore, it was regarded that the thickness could affect the ionic conductivity of the protective layer. So, we made the film as thin as possible and the average thickness of protective

layer is 8 um. The effect of the c-PEGDMA protective layer on the Li metal surface after 100 cycles is shown in Figure 4.6g. Unlike the bare Li metal surface, the c-PEGDMA-coated surface did not show cracks or a degraded electrolyte. In the wrinkled c-PEGDMA protective film, the segment of PEGDMA is extended to suppress the volume expansion. The cross-sectional image in Figure 4.6h shows a dramatic change compared to the surface of the bare Li metal. The Li metal with a c-PEGDMA protective film exhibits a thickness of 34.7 μm, which is increased by 26.7 μm. This increase is smaller than the increase (>100 μm) for the bare Li metal by a factor of about three. Moreover, the growth of dendritic structures seen on the bare Li metal is not observed. Thus, it is confirmed that the c-PEGDMA protective film structure can dramatically suppress electrolyte decomposition due to volume expansion.

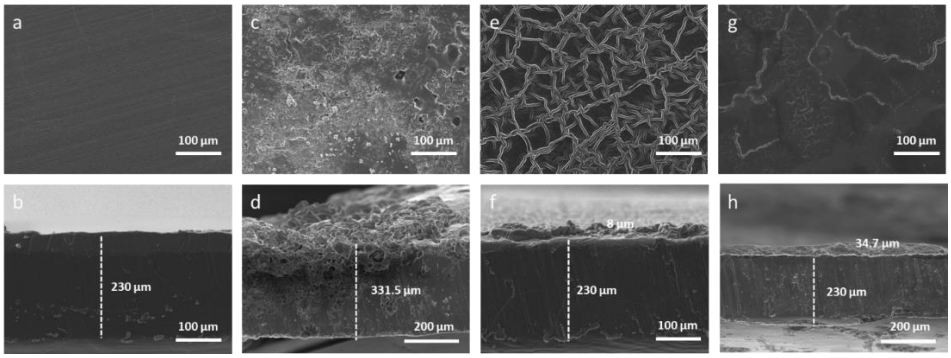

Figure 4.6 SEM images of the surface of bare Li metal (a) and cross-section (b). Bare Li metal images after 100 cycles (c) and cross-section (d). SEM images of the surface of PEGDMA protective layer applied Li metal (e) and cross-section (f). PEGDMA protective layer applied Li metal after 100 cycles (g) and cross-section (h).

The symmetrical cell test was conducted to verify the stabilization performance of c-PEGDMA on Li metal surfaces. [23] If the SEI layer was broken by the volume expansion of the Li metal, another SEI layer was formed to replace it, and the stacked electrolyte decomposition layers acted as a resistive component to increase the voltage range. [10] Li-ion plating-stripping current density conditions were performed at 1 and 5 mA cm^{-2}. The black line in Figure 4.7a shows that the voltage of the bare Li metal increased with the resistance associated with the stacked electrolyte decomposition layer on the surface. After 280 h, the voltage dropped rapidly and then rose again. The voltage drop corresponded to crack formation in the SEI layer because of the volume expansion of the Li metal; the crack formation reduced the resistance instantaneously for a moment. Subsequently, the crack was covered and the SEI acquired its original level of resistance. However, an unstable surface eventually results in short circuits because of dendrite growth. [24] By contrast, the Li metal with a c-PEGDMA protective film (Figure 4.7a, red line) suppressed the phenomenon of recovering by breaking the SEI layer formed by volume expansion, and showed stable performance even after 500 h. A specific section of the 50 and 200 h showed that the Li metal with c-PEGDMA had lower polarization than the bare Li metal surface (Figure 4.8). The voltage hysteresis was calculated using the following expression, for performing an accurate comparison. [10]

$$\text{Voltage hysteresis} = \frac{V_{Max_{stripping}} - V_{min_{plating}}}{2}$$

The Li metal with a c-PEGDMA coating exhibited a voltage hysteresis of 1.0 mV, but the bare Li metal showed 400 mV (Figure 4.9). The experiment was conducted at a current density that was five times greater than 1 mA cm^{-2} (Figure 4.7b). For the current density of 5 mA cm^{-2}, the bare Li metal exhibited a more unstable behavior at the beginning compared with its behavior at 1 mA cm^{-2}, and cell failure occurred. However, when c-PEGDMA was coated on the Li metal, it showed stable behavior even after 500 h of plating and stripping. Figure 4.10 clearly shows the stable behavior of the voltage profile. The voltage hysteresis of the Li metal with c-PEGDMA was 2.5 mV, which is very small compared to the value of 1200 mV observed for the bare Li metal (Figure 4.11). The above results demonstrate that the c-PEGDMA protective film effectively inhibits electrolyte degradation on Li metal at various current densities.

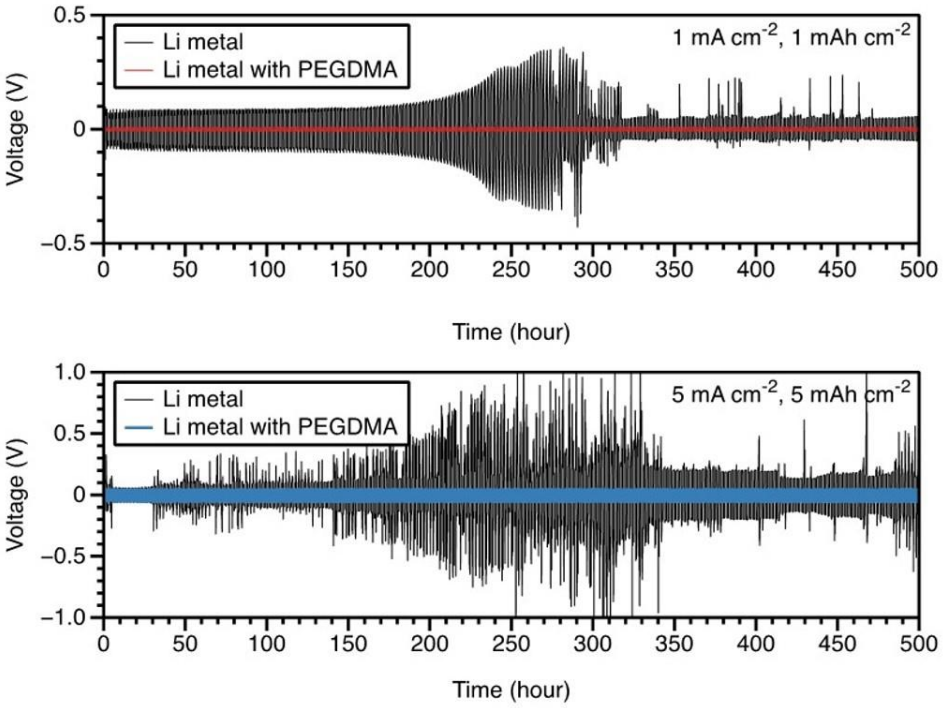

Figure 4.7 (a) The voltage profile of symmetrical cell tests with the bare Li metal (black) and Li metal with PEGDMA (red) for 500 hours at 1 mA cm^{-2}. And (b) the voltage profile of symmetrical cell tests with the bare Li metal (black) and Li metal with PEGDMA (blue) for 500 hours at 5 mA cm^{-2}.

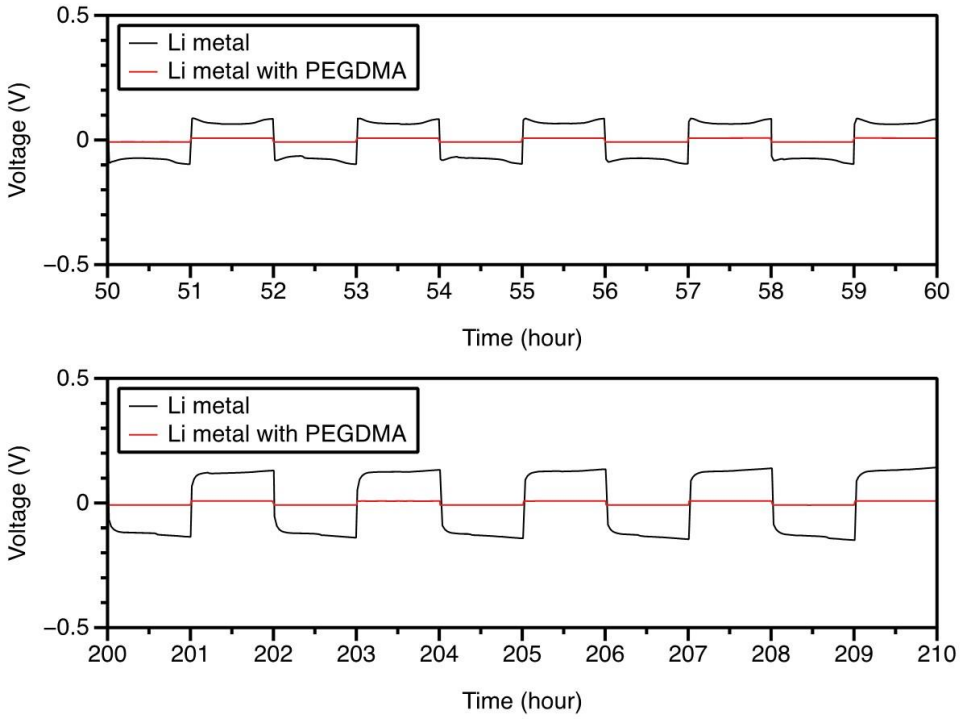

Figure 4.8 The voltage profile of symmetrical cell tests with the bare Li metal (black) and Li metal with PEGDMA (red) at 50~60 h (upper) and 200~210 h (lower) with 1mA cm^{-2}

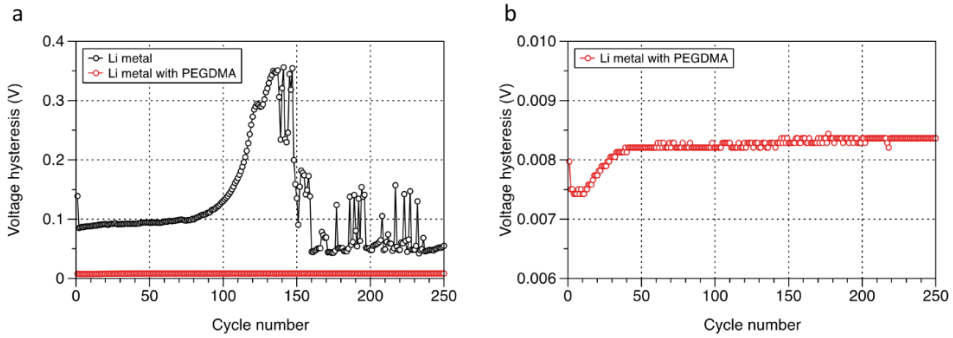

Figure 4.9 (a) The voltage hysteresis of Li metal (black) and Li metal with PEGDMA (red) at 1mA cm^{-2} (b) The voltage hysteresis of Li metal with PEGDMA at 1mA cm^{-2}

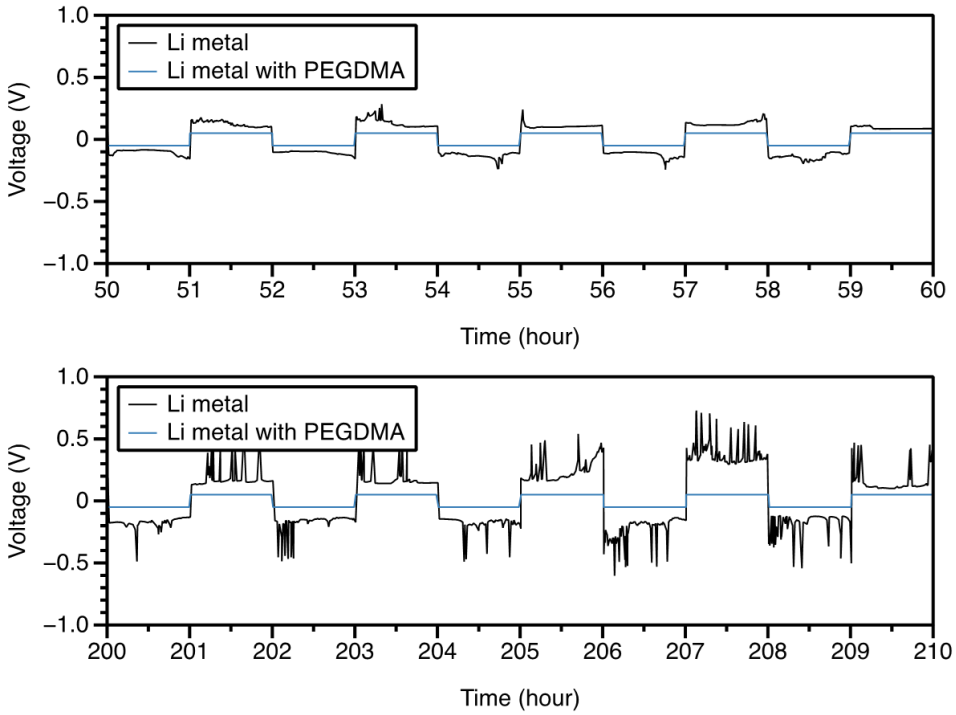

Figure 4.10 The voltage profile of symmetrical cell tests with the bare Li metal (black) and Li metal with PEGDMA (blue) at 50~60 h (upper) and 200~210 h (lower) with 5 mA cm^{-2}

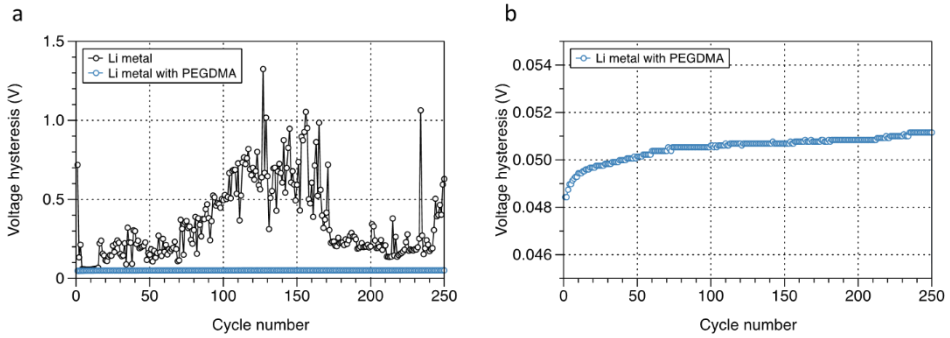

Figure 4.11 (a) The voltage hysteresis of Li metal (black) and Li metal with PEGDMA (blue) at 5mA cm^{-2} (b) The voltage hysteresis of Li metal with PEGDMA at 5 mA cm^{-2}

X-ray photoelectron spectroscopy (XPS) was performed with monochromatic Al Kα radiation (hν = 1486.7 eV) to examine the surface stability of the bare and coated Li metals after 100 cycles. The pressure in the analysis chamber was 10−9 to 10−8 mbar. According to the XPS spectra in Figure 4.12, the surface of the Li metal with PEGDMA comprised only C and O. The PEGDMA film signals at 284.8, 286.8, and 289.1 eV correspond to C–C/C–H, C–O, and O[double bond, length as m-dash]C–O bonds, respectively. [25,26] For Li metal with c-PEGDMA, after 100 cycles, the C1s XPS spectra showed a reduction in the C–O peak and an increase in the C–C and C–H peaks (Figure 4.13e). An increase in the C–O peak indicates the presence of residues of the electrolyte, such as ethylene carbonate and diethyl carbonate, despite the surface having been washed with diethyl carbonate. The C1s spectra of the bare Li metal obtained after 100 cycles show peaks at 284.8, 286.8, and 290.3 eV, consistent with the C–O groups of Li_2CO_3 or Li alkyl carbonate ($ROCO_2Li$) and CO_3^{2-}, which was formed by the decomposition of the electrolyte. [25-27] This result is also consistent with the 55.0 ($ROCO_2Li$) and 55.5 eV (Li_2CO_3) peaks of the Li1s spectra. In the P2p spectra of Figure 4.13b and f, the peak at 134.3 eV (phosphates) is related to the decomposition of $LiPF_6$. [28] Even if the Li metal is washed with diethyl carbonate and dried, residue from the decomposition is observed on the surface at 134.0 eV. A comparison of the intensities of spectra shows that the amount of decomposed electrolyte on the surface of PEGDMA is smaller than the amount of $LiPF_6$, and the phosphate content is higher for the bare Li metal. The F1s spectra (Figure 4.13c and g) show peaks at 685.2, 687.0, and

688.3 eV, corresponding to LiF, Li_xPF_y, and $LiPF_6$, respectively. [34,35] LiF and Li_xPF_y were products of the reduction of $LiPF_6$, which occurs as follows. [28]

$$LiPF_6 \xrightarrow[\mathrm{n}Li^+,ne^-]{} \mathrm{n\ LiF} + Li_xPF_y$$

LiF is also observed in the Li1s spectra. A LiF-rich SEI layer suppresses dendrite growth induced by uneven Li-ion deposition. [29,30] While for the bare Li metal, electrolyte decomposition products such as $ROCO_2Li$ (55.0 eV) and Li_2CO_3 (55.5 eV) were observed (Figure 4.13d), only LiF was observed for the Li metal with c-PEGDMA (Fig. 4h). The above equation can differs in degree of decomposition depending on the state of stabilization of the Li metal surface, and the relative component contents can be changed in the washing process from XPS sampling with diethyl carbonate. Because of the limited penetration depth of the XPS, measuring the surface of the sample is more likely to measure the c-PEGDMA surface than the SEI layer. [31,32] However, on the basis of the electrolyte by-products remaining on the surface following the volume expansion of the Li metal, we can infer that the c-PEGDMA protective film inhibits the volume expansion and electrolyte degradation. A naked-eye inspection of the XPS images of the coated and bare Li metal samples in Figure 4.14 shows that both samples are almost identical, with the bare sample being covered with the decomposed electrolyte.

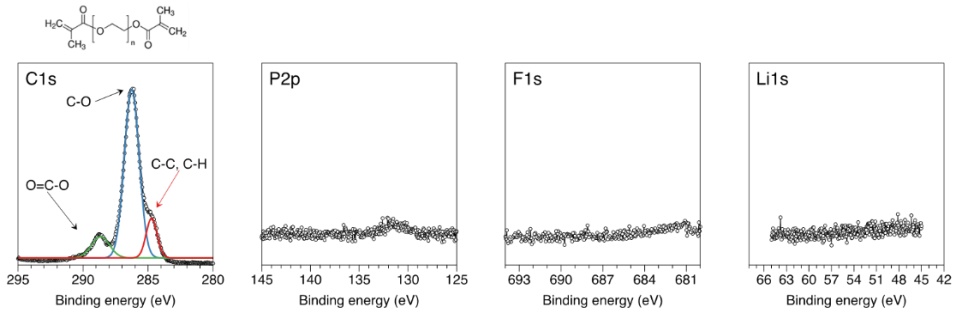

Figure 4.12 C1s, P2p, F1s, and Li1s XPS core spectra of Li metal with PEGDMA without cycle.

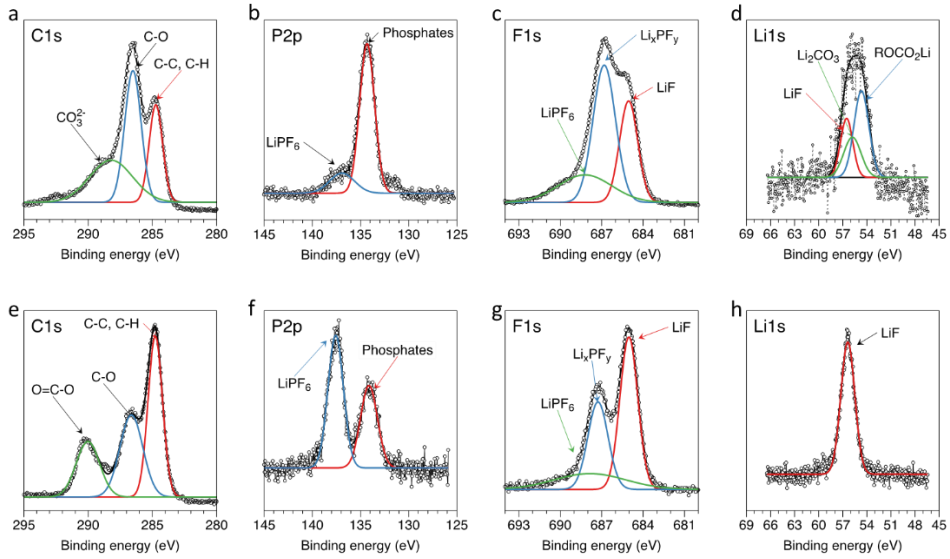

Figure 4.13 C1s, P2p, F1s, and Li1s XPS core spectra of (a–d) the bare Li metal and (e–h) the Li metal with c-PEGDMA after 100 cycles.

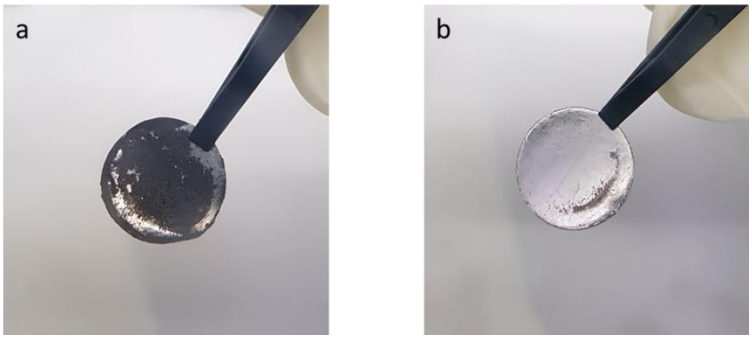

Figure 4.14 (a) Surface image of Li metal sample after 100 cycles, (b) Surface image of Li metal with PEGDMA sample after 100 cycles.

4.2.4 Effect of PEGDMA protective layer for Li metal battery

To evaluate the application of the proposed film to an actual cell system, the $LiFePO_4$/Li metal test was performed by using $LiFePO_4$ as the cathode material because of its stability. [33] The C-rate results were similar for both coated with c-PEGDMA and bare Li metal (Figure 4.15a and b). The c-PEGDMA film coated on the surface was 8.0 μm thick, and therefore, it could act as a surface resistance component. However, as indicated by the electrochemical impedance spectroscopy data presented earlier in this paper, it does not interfere with the electrochemical reaction on its surface and shows a consistent level of performance at high C-rates such as 2 and 5C. A comparison of the initial capacity with the capacity at a later instant at 0.2C shows that both capacities are comparable (Figure 4.15c). On the basis of these results, cycle tests were conducted to confirm the long-term stability. The capacity in the first cycle was similar, but the capacity changed as the charge–discharge process progressed, and the final capacity after 250 cycles was around three times the initial capacity. As shown in Figure 4.15e, without a protective layer, the capacity retention and coulombic efficiency were 12.9% and 89.8%, respectively. By contrast, the Li metal with a c-PEGDMA protective film showed a capacity retention of 36.9% compared to the initial capacity and a coulombic efficiency of 95.5%. Charge/discharge profiles for 100 cycles at 5C are shown in Figure 4.16. The cycle test was also conducted at 1C (Figure 4.17). When bare Li metal was used, the capacity, which was initially 142.10 mA h g^{-1}, continuously decreased, reaching 3.28 mA h g^{-1} at 400 cycles. The coulombic efficiency

decreased sharply after 300 cycles, and fluctuated between 60% and 70%. By contrast, c-PEGDMA showed a capacity that was 10 times higher, 32.80 mA h g^{-1}, after 400 cycles and maintained a coulombic efficiency of 89.4%. Charge/discharge profiles for 100 cycles at 1C are shown in Figure 4.18. These results showed the high stability of the PEGDMA protective film in the $LiFePO_4$/Li metal tests.

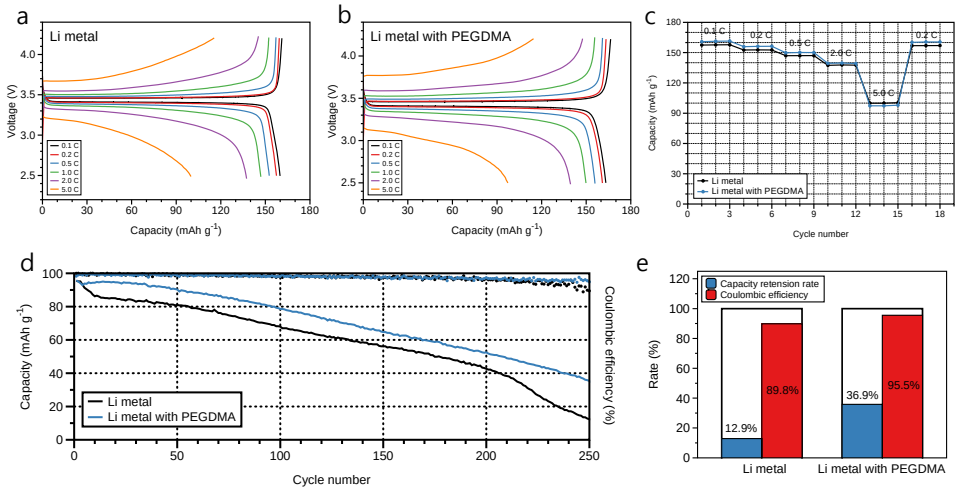

Figure 4.15 Charge/discharge profile of $LiFePO_4$ sample with bare Li metal (a) and coated with c-PEGDMA (b) at 0.1C (black), 0.2C (red), 0.5C (blue), 1.0C (green), 2.0C (purple) and 0.5C (yellow). (c) The rate capability at varieties C-rate. (d) The graph of cycle stability at 5.0C. (e) Capacity retention rate and coulombic efficiency of Li metal and coated with c-PEGDMA at 5.0C.

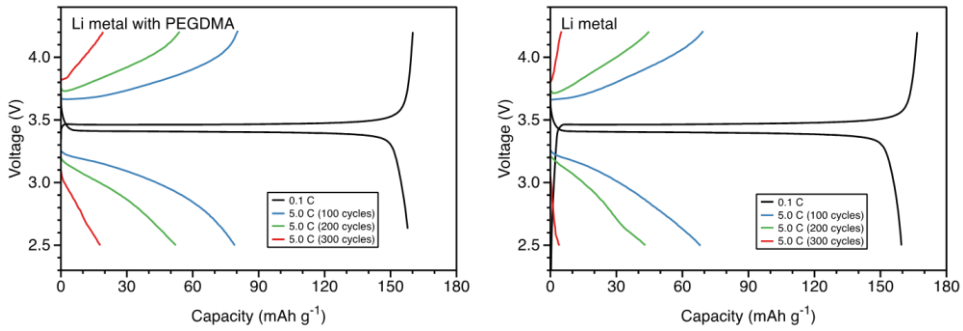

Figure 4.16 Charge/discharge profile of $LiFePO_4$ sample with bare Li metal (a) and Li metal applied PEGDMA (b) at 0.1C and 1.0C after 100, 200, and 300 cycles.

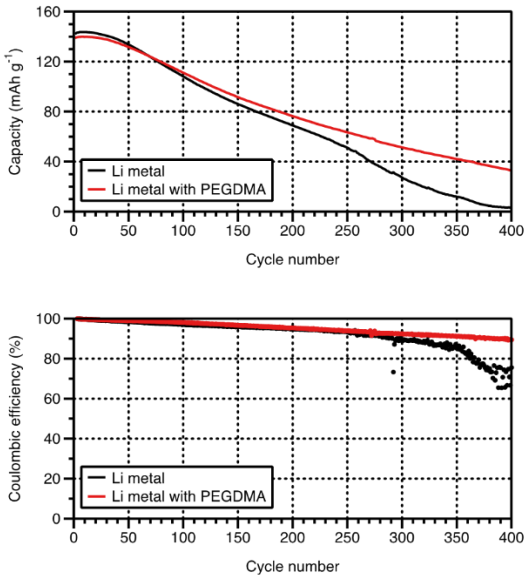

Figure 4.17 The graph of cycle capacity (upper) and Coulombic efficiency (lower) at 1.0C

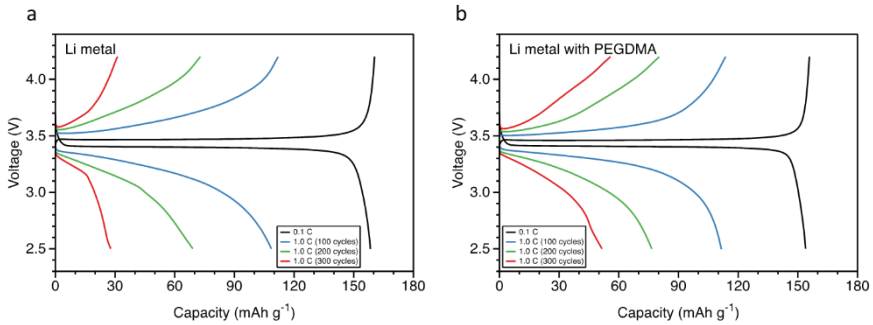

Figure 4.18 Charge/discharge profile of $LiFePO_4$ sample with bare Li metal (a) and Li metal applied PEGDMA (b) at 0.1C and 5.0C after 100, 200, and 300 cycles.

The applicability of the c-PEGDMA protective layer to pouch cells was examined. Pouch cells were tested to ensure that the system of PEGDMA protective layer was applicable in large scale. In the preparation of a pouch cell sample, a c-PEGDMA film was bar coated on the Li metal surface. The pouch sample is shown in Figure 4.19a. The rate capability of the cell was determined, and it was comparable to that of a coin cell (Figure 4.20). Because of the flexibility of the c-PEGDMA protective layer, the LED lamp was turned on even if the sample was bent (Figure 4.19b) or folded (Figure 4.19c). The proposed simple method can be used to easily manufacture stable Li metal batteries by coating c-PEGDMA in the roll-to-roll process.

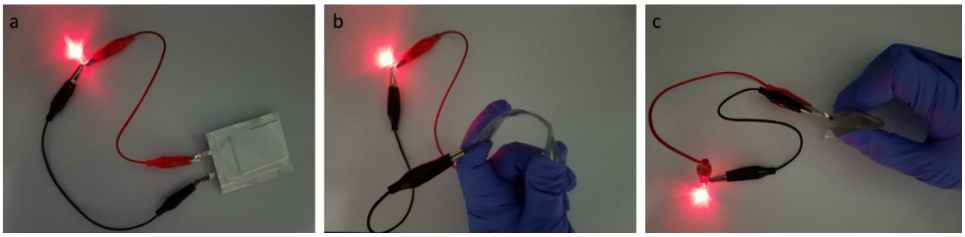

Figure 4.19 Pictures of pouch cell (a). And picture of pouch cell when bent (b) and folded (c).

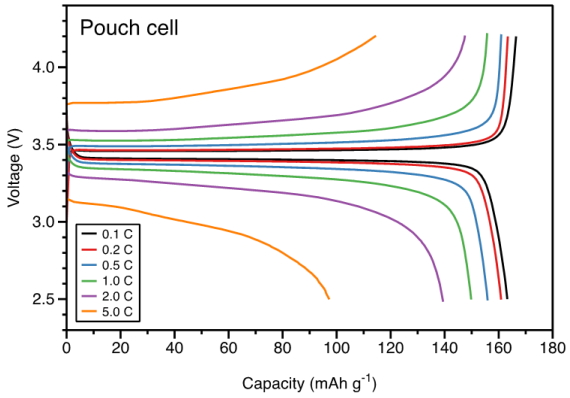

Figure 4.20 Charge/discharge profile of $LiFePO_4$ pouch sample with bare Li metal with PEGDMA

4.3 Conclusion

In summary, we propose a simple process for coating c-PEGDMA and a thermal initiator through bar coating on Li metal and fabricating a c-PEGDMA film at 100 °C in a short time without requiring any solvent. In a symmetrical cell test performed at 1 and 5 mA cm^{-2}, the c-PEGDMA protective film produced by this process showed long-term stability. SEM and XPS measurements confirmed that the c-PEGDMA protective film effectively inhibited the volume expansion of Li metal, thereby suppressing the degradation of the surface SEI layer and stabilizing the surface. Impedance tests confirmed that the use of polymeric materials, such as c-PEGDMA with ethylene oxide units, provided flexible mechanical strength and also played a role in Li-ion transfer. In an $LiFePO_4$/Li metal cell, a c-PEGDMA protective film on the Li metal surface showed similar capacity at high C-rates and long-term cycle stability. Furthermore, it was observed that when a c-PEGDMA coating was provided to the Li metal in a pouch cell, the effect of the coating persisted even when the cell was bent or folded. With the increasing demand for large-capacity batteries necessitating the development of next-generation batteries, appropriate engineering of Li metal surfaces can help to realize next-generation batteries. The proposed c-PEGDMA coating method is simple and effective.

4.4 Experimental details

Materials

Poly (ethylene glycol) dimethacrylate (M_n 550, Sigma-Aldrich) was used as polymer film of protective layer. And tert-Butyl pivalate (Sigma-Aldrich) was employed as initiator of radical polymerization. Lithium (MTI Korea) was used as working, reference and counter electrode. The separator of polyethylene (20 μm) and electrolyte of 1 M $LiPF_6$ in EC (ethylene carbonate)/DEC (diethyl carbonate) (50/50 by volume, 50 mL) were obtained from Asahi Kasei Chemicals Corporation and PANAX ETEC Co. Ltd, respectively. $LiFePO_4$ (Hanwa Chemicals), PVdF (arkema) and Super P (MTI korea) were employed as cathode material.

Preparation of PEGDMA protective layer

0.01 g of tert-Butyl peroxypivalate was added into 1 g of poly (ethylene glycol) dimethacrylate. This solution was stirring at room temperature and dropped onto lithium metal surface. This droplet coated with the bar coater to make a film on the lithium metal surface. After casting process, polymerization of Poly (ethylene glycol) dimethacrylate was obtained for 1 minute with 100 ℃ on hot plate. Manufacturing processes of PEGDMA protective layer were performed in an argon-filled glove box.

Preparation of $LiFePO_4$ electrode

The cathode materials were prepared by mixing the $LiFePO_4$, super P and poly-(vinylidene fluoride) in a weight ratio of 8:1:1 in N-methyl pyrrolidone to ensure homogeneity. This slurry was coated on an Aluminum foil (18 um) and dried under the convection oven at 120 ℃ for 2 h and the vacuum oven at 120 ℃ for 12 h. Then the electrode foil was cut with 16 mm in diameter. The loading density of this electrode is 1.8 mg cm^{-2}.

Electrochemical measurements

Coin cells (CR2032) were assembled to evaluate stability of Li metal surface after galvanostatic charge and discharge. All processes were carried out in an argon-filled glove box. In symmetrical cell test, Li metal is working electrode. Also, Li metal is counter and reference electrode. PE separator and 1M $LiPF_6$ in EC/DEC were used as separator and electrolyte, respectively. Cell tests were conducted with a current density of 1, 5 mA cm^{-2}. The charge and discharge time are 1 hour each. After cycle test is completed, the cell is opened with a scissor in a glove box, then washed with a few drops of diethyl carbonate (DEC) to measure SEM and XPS. To evaluate the rate capability, LFP/Li test was investigated. First cycle was performed with 0.1 C. Then, this cell was cycled in different C rates such as 0.2 C, 0.5 C, 1.0 C, 2.0 C, and 5.0 C respectively. Finally, 0.2c was performed to estimate the capacity recovery rate.

4.5 References

[1] M. Armand, Nature, 2001, 414, 359–367.

[2] S. Chu and A. Majumdar, Nature, 2012, 488, 294–303.

[3] B. Dunn, H. Kamath and J. M. Tarascon, Science, 2011, 334, 928–935.

[4] D. Lin, Y. Liu and Y. Cui, Nat. Publ. Gr., 2017, 12, 194–206.

[5] B. Liu, J. G. Zhang and W. Xu, Joule, 2018, 2, 833–845.

[6] W. Xu, J. Wang, F. Ding, X. Chen, E. Nasybulin, Y. Zhang and J. G. Zhang, Energy Environ. Sci., 2014, 7, 513–537.

[7] E. Peled and S. Menkin, J. Electrochem. Soc., 2017, 164, A1703–A1719.

[8] I. Warshawsky, J. Electrochem. Soc., 1980, 127, 1324.

[9] K. Liu, A. Pei, H. R. Lee, B. Kong, N. Liu, D. Lin, Y. Liu, C. Liu, P. chun Hsu, Z. Bao and Y. Cui, J. Am. Chem. Soc., 2017, 139, 4815–4820.

[10] H. Kim, Y. J. Gong, J. Yoo and Y. S. Kim, J. Mater. Chem. A, 2018, 6, 15540–15545.

[11] D. Lin, J. Zhao, J. Sun, H. Yao, Y. Liu, K. Yan and Y. Cui, Proc. Natl. Acad. Sci., 2017, c, 201619489.

[12] E. Cha, M. D. Patel, J. Park, J. Hwang, V. Prasad, K. Cho and W. Choi, Nat. Nanotechnol., 2018, 13, 337–343.

[13] Y. Liu, D. Lin, P. Y. Yuen, K. Liu, J. Xie, R. H. Dauskardt and Y. Cui, Adv. Mater., 2017, 29, 1–8.

[14] J. Lopez, D. G. Mackanic, Y. Cui and Z. Bao, Nat. Rev. Mater., 2019, 4, 312–330.

[15] J. Lopez, A. Pei, J. Y. Oh, G. J. N. Wang, Y. Cui and Z. Bao, J. Am. Chem. Soc., 2018, 140, 11735–11744.

[16] R. Xu, X. Q. Zhang, X. B. Cheng, H. J. Peng, C. Z. Zhao, C. Yan and J. Q. Huang, Adv. Funct. Mater., 2018, 28, 1–7.

[17] B. Zhu, Y. Jin, X. Hu, Q. Zheng, S. Zhang, Q. Wang and J. Zhu, Adv. Mater., 2017, 29, 2–7.

[18] D. Bresser, S. Lyonnard, C. Iojoiu, L. Picard and S. Passerini, Mol. Syst. Des. Eng., 2019, 4, 779–792.

[19] W. H. Meyer, Adv. Mater., 1998, 10, 439–448.

[20] Z. Xue, D. He and X. Xie, J. Mater. Chem. A, 2015, 3, 19218–19253.

[21] G. Socrates, Infrared and Raman Characteristic Group Frequencies: Tables and Charts, John Wiley & Sons Ltd., Chichester, 3rd edn, 2001.

[22] Q. Li, S. Zhu and Y. Lu, Adv. Funct. Mater., 2017, 27, 1606422.

[23] H. Wang, D. Lin, Y. Liu, Y. Li and Y. Cui, Sci. Adv., 2017, 3, 1–10.

[24] C.-P. Yang, Y.-X. Yin, S.-F. Zhang, N.-W. Li and Y.-G. Guo, Nat. Commun., 2015, 6, 8058.

[25] P. Shi, H. Zheng, X. Liang, Y. Sun, S. Cheng, C. Chen and H. Xiang, Chem. Commun., 2018, 54, 4453–4456.

[26] S. Leroy, F. Blanchard, R. Dedryvère, H. Martinez, B. Carré, D. Lemordant and D. Gonbeau, Surf. Interface Anal., 2005, 37, 773–781.

[27] J. Zheng, P. Yan, R. Cao, H. Xiang, M. H. Engelhard, B. J. Polzin, C. Wang, J. G. Zhang and W. Xu, ACS Appl. Mater. Interfaces, 2016, 8, 5715–5722.

[28] B. S. Parimalam and B. L. Lucht, J. Electrochem. Soc., 2018, 165, A251–A255.

[29] J. Ko and Y. S. Yoon, Ceram. Int., 2019, 45, 30–49.

[30] J. Zhao, L. Liao, F. Shi, T. Lei, G. Chen, A. Pei, J. Sun, K. Yan, G. Zhou, J. Xie, C. Liu, Y. Li, Z. Liang, Z. Bao and Y. Cui, J. Am. Chem. Soc., 2017, 139, 11550–11558.

[31] V. Eshkenazi, E. Peled, L. Burstein and D. Golodnitsky, Solid State Ionics, 2004, 170, 83–91.

[32] P. J. Cumpson, Appl. Surf. Sci., 1999, 144–145, 16–20.

[33] L. X. Yuan, Z. H. Wang, W. X. Zhang, X. L. Hu, J. T. Chen, Y. H. Huang and J. B. Goodenough, Energy Environ. Sci., 2011, 4, 269–284.

[34] Z. Peng , N. Zhao , Z. Zhang , H. Wan , H. Lin , M. Liu , C. Shen , H. He , X. Guo , J. G. Zhang and D. Wang , Nano Energy, 2017, 39 , 662–672.

[35] Y. Yuan , F. Wu , Y. Bai , Y. Li , G. Chen , Z. Wang and C. Wu , Energy Storage Materials, 2019, 16 , 411–418.

Chapter 5 In situ LiF protective layer

5.1 Introduction

With the advent of the electric vehicle era, the demand for large-capacity batteries is increasing. [1,2] Consumers hope that they can drive longer distances on a full charge. However, capacity of existing lithium-ion batteries is theoretically limited. [2] Among the possible alternatives, lithium metal is most promising owing to its highest theoretical capacity (3860 mAh g^{-1}) and lowest electrode potential (-3.04 V vs. standard hydrogen electrode) of Li metal. [3-5] When a Li metal battery is in operation. A solid electrolyte interphase (SEI) layer is formed on the surface of Li metal as the electrolyte decomposes, as shown in Figure 5.1a. [3,6,7] However, because Li metal is a "host-less" material, the SEI layer cracks easily because of huge volume expansion. [4,5,8] When the SEI layer is cracked, Li-ion flux increases at the cracks, where resistance to ion movement decreases instantly, and dendrites are formed. [8] When these dendrites grow, they penetrate the membrane and come into contact with the cathode, which introduces the risks of short circuit and fire. The freshly formed SEI layer at the cracks consumes additional electrolytes and forms dead Li, which is a major cause of low Coulombic efficiency and rapid capacity degradation. [9] Owing to these problems, Li metal batteries have not been commercialized. To solve these problems, various studies have been conducted. [9-11] Among them, the most remarkable solution involves stabilizing the SEI layer of

Li metal. [12-15] Lithium fluoride (LiF) is the main element in the inorganic part of the SEI layer, which is naturally formed between organic electrolytes and Li metal. LiF does not have high ionic conductivity, but it exhibits high levels of chemical stability compared to the other components of the SEI layer. [13] For these reasons, many studies have reported that the performance of Li metal can be effectively improved by coating an SEI layer containing LiF on its surface on its surface. [13-16] These studies can be classified into two categories: first, coating on Li metal surface with a mixture of LiF and polymer dissolved in a solvent to form a LiF layer [14,16] and second, injecting a gaseous LiF precursor into the Li metal surface. [17] By using the conventional fabrication methods of the artificial SEl layer, it is difficult to distribute LiF thinly and uniformly on the surface of Li metal, and a process of drying solvent is required. The method of flowing in a gaseous state is an expensive process.

In this chapter, we describe the synthesis of an “in situ LiF PL” that employs 2-(perfluorooctyl)ethyl acrylate (Figure 5.1b). 2-(perfluorooctyl)ethyl acrylate is coated on the Li metal surface by using an initiator and cured at 60 °C for 1 min to form LiF on the surface, as shown in Figure 5.1c. This process does not require any binder or solvent. In the curing process, tert-Butyl peroxypivalate is used as the initiator. 2-(perfluorooctyl)ethyl acrylate is cured by the free radicals in tert-Butyl peroxypivalate and forms a film on the metal surface. This F-rich film provides the F required for the formation of LiF in the artificial SEI layer. [16] The resulting LiF layer on the surface of Li metal inhibits dendrite growth and enhances the stability of the Li metal interface.

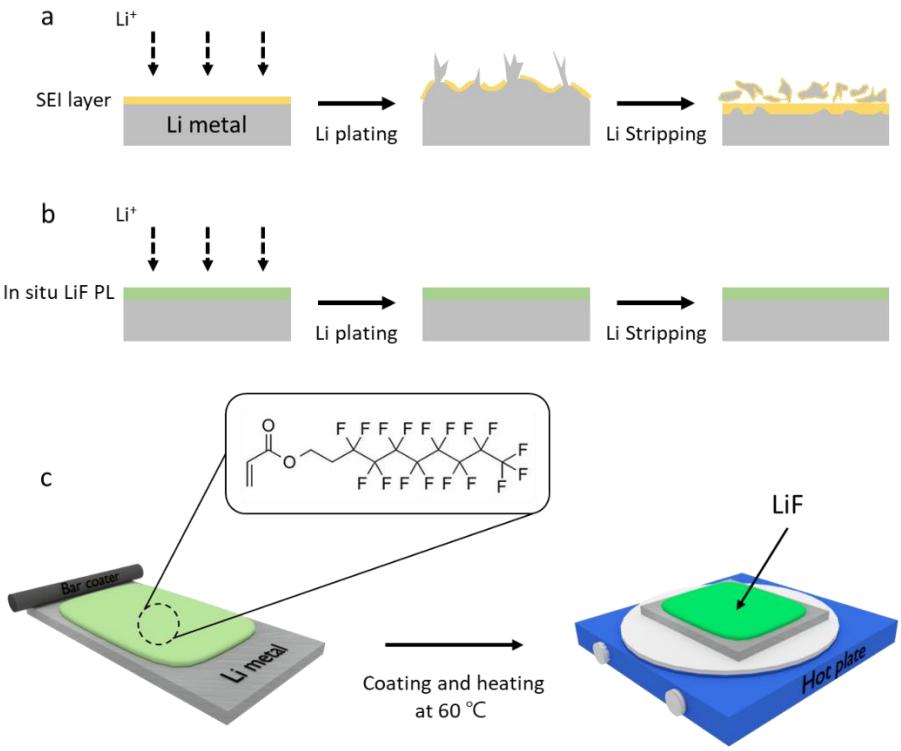

Figure 5.1 Comparison between bare Li metal and Li metal with F-rich protective layer during Li plating and stripping. (a) Bare Li metal after Li plating and stripping. (b) Li metal with F-rich protective layer after Li plating and stripping. (c) Schematic illustrations of the fabrication of in situ LiF protective layer.

5.2 Experimental section

5.2.1 Fabrication of in situ LiF protective layer

2-(perfluorooctyl)ethyl acrylate (Fluoryx Labs) was used as the PL. Tert-Butyl peroxypivalate (Sigma Aldrich) was used as the initiator. 2-(perfluorooctyl)ethyl acrylate and tert-Butyl peroxypivalate were mixed in a mass ratio of 10:1 to form the curing mixture.

5.2.2 Characterization of in situ LiF protective layer

The F-rich material was analyzed with attenuated total refection infrared spectroscopy (ATR-FTIR), as shown in Figure 5.2a. The absorption peaks located at 1092–1257 cm^{-1} indicate the C–F bonding in cross-linked F-rich material. [11] Peaks at 1607–1653 cm^{-1} and 1708-1766 cm^{-1} denote C=C stretching and C=O stretching in the acrylate group, respectively. [18] The peak intensity of C=C significantly decreased after the cross-liking reaction. This means that the F-rich material can be produced into a film through thermal curing. The F-rich material cured on the Li metal surface was analyzed with X-ray photoelectron spectroscopy (XPS) measurement (Figure 5.2b-e). When C–F bonds meet metallic Li, which is a strong electron donor, they break and form LiF. [17] The F-rich film coated on the surface of Li metal forms LiF according to this mechanism. The C1s spectrum of

the F-rich film coated on the Li metal surface exhibited peaks at 284.8, 286.8, 289.1, and 290.7 eV corresponding to C–C/C–H, C–O, O=C–O, and CF_n bonds, respectively (Figure 5.2b). [19-24] These peaks can be ascribed to crosslinked 2-(perfluorooctyl)ethyl acrylate. The F1s spectrum of the film contains peaks at 685.2 eV and 688.1 eV corresponding to LiF and CF_n, respectively (Figure 5.2c). [24] The Li1s spectrum contains the LiF peak, as was confirmed by the F1s spectrum (Figure 5.2d). Figure 5.3 illustrates the atomic percentages in the XPS results. Based on the proportions of LiF in the F1s and Li1s spectra and the corresponding atomic percentages, we presumed that LiF was formed with a high ratio. Consequently, it was confirmed that the F-rich film cured on the Li metal surface broke C–F bonds and formed LiF. To confirm the uniformity of the in situ LiF PL coated on the Li metal surface, EDS mapping was conducted (Figure 5.4). The distribution of C, O, and F elements shows that the in situ LiF PL spread evenly without any aggregation. X-ray diffraction (XRD) was additionally performed to confirm the crystallinity of the formed LiF shown in Figure 5.5. When the lithium metal surface was measured, two theta was confirmed at the positions of Li (110), Li (200), and Li (211). When the in situ LiF PL was coated on Li metal, Li peaks were observed at the same degree, but the intensity was reduced due to being covered by the in situ LiF PL. In addition, LiF (111) and LiF (200) peaks were observed at 38.33° and 45°, respectively, which indicate the crystallinity of LiF. [31] It was found that the LiF structure was formed on the surface of the lithium metal, although the intensity was weak. Both samples were exposed to air. Therefore, an LiOH peak due to moisture was observed.

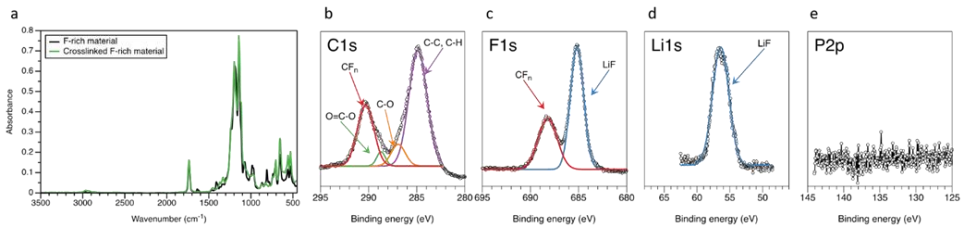

Figure 5.2 (a) Attenuated total reflectance Fourier transform infrared (ATR-FTIR) spectra of the F-rich material. (b–e) X-ray photoelectron spectroscopy (XPS) spectra of the F-rich film coated on the Li metal surface.

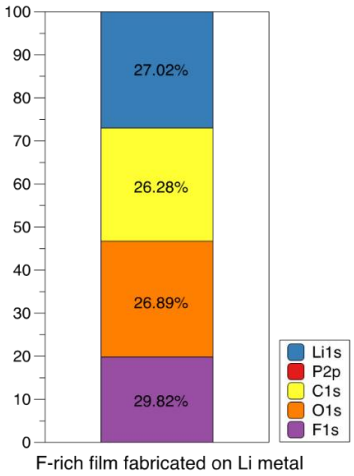

Figure 5.3 Atomic percentages of F-rich film fabricated on Li metal surface.

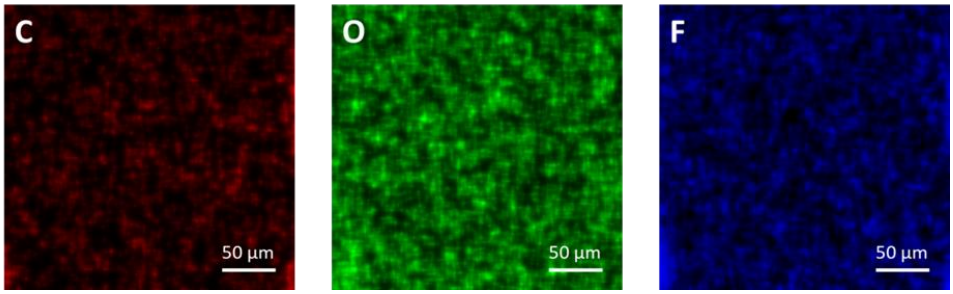

Figure 5.4 Energy-dispersive X-ray spectroscopy (EDS) mapping images of in situ LiF PL on Li metal

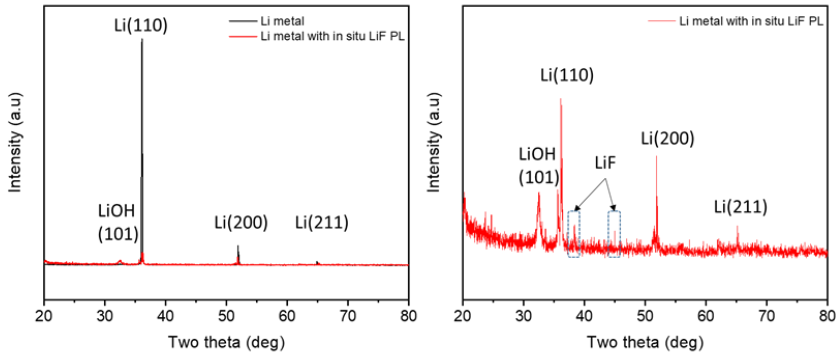

Figure 5.5 X-ray diffraction (XRD) analysis of in situ LiF PL on Li metal

5.2.3 Surface analysis and electrochemical measurement

A symmetrical cell test was performed to analyze the Li metal surface. Working, counter, and reference electrodes made of Li metal were used in the experiment. 1M $LiPF_6$ in ethylene carbonate (EC)/diethyl carbonate (DEC) and polyethylene (PE) film were used as the electrolyte and the separator, respectively. The cell was charged with a current density of 1 mA cm^{-2} for 1 h and subsequently discharged for 1 h. The experimental results of scanning electron microscopy (SEM) are shown in Figure 5.6a-d (SEM images consist of a cross-sectional photograph and a surface photograph on the upper left side). The surface of the bare metal can be seen in the horizontal pattern generated during the surface manufacturing process, and the thickness of the cross-section is 230 μm. [11,25] The results obtained using bare Li metal over 100 cycles are illustrated in Figure 5.6b. The horizontal pattern in Figure 5.6a cannot be found in Figure 5.6b owing to dendrite growth and dead Li generation due to volume expansion of Li metal. The thickness of the cross section is 348 μm, which is approximately 1.5 times greater than the initial thickness of 230 μm. In addition, multiple cracks can be observed in the cross-sectional image. The results of application of the in situ LiF PL to the surface of Li metal are shown in Figure 5.6c. Although the in situ LiF PL was coated on the surface, it barely changed the surface properties and thickness. Various experiments were conducted to confirm the thickness of the in situ LiF PL, but the measurement was difficult due to the ductility and reactivity of Li metal. So, a Cu/Li (Li deposited on a copper

surface) sample whose thickness is easy to control is used. The thickness of the Cu/Li single layer is 34 μm (Figure 5.7a). When 10 layers are stacked, the thickness is 340 μm (Figure 5.7b). The thickness of 10 layers coated with the in situ LiF PL increased by 1 μm (Figure 5.7c). Therefore, it can be seen that the thickness of the in situ LiF PL is 0.1 μm. When the Li metal samples coated with the in situ LiF PL on their surface were subjected to energy-dispersive X-ray spectroscopy (EDS) measurements for comparison with bare Li metal, F was observed only on the surface coated with the in situ LiF PL (Figure 5.8). The reported polymer structure embedded with LiF had a thickness of 0.1 μm, which can reduce the volumetric energy density [14,16] Moreover, this design can minimize the loss of volumetric energy density. The results obtained for the Li metal surface coated with the situ LiF PL over 100 cycles are shown in Figure 5.6d. In contrast with bare Li metal over 100 cycles, dendrite growth and dead Li were not found. The cross-sectional thickness increased by only 29 μm compared to the initial thickness of Li metal. This is approximately four times lower than the 118 μm increase in cross-sectional thickness compared to the initial value in the case of bare Li metal. The differences in the Li metal surface are dramatic, even to the naked eye (Figure 5.9). Figure 5.6e shows the voltage profile obtained for the applied current density of 1 mA cm^{-2}. As the SEI layer cracks owing to volume expansion of Li metal, a new SEI layer is formed to recover it, and the destroyed SEI layer is stacked on the surface. The accumulated destroyed layers on the surface of L metal act as a resistor and increase the voltage even when the same current density is applied. [9-11] Therefore, the increase in voltage indicates instability of the surface, which is analogous to the

increase in thickness, manifested as a rough surface, in the SEM results. The bare Li metal and the Li metal with in situ LiF PL samples exhibited similar voltages in the early stages, but the voltage of the bare Li metal sample increased gradually after 50 h of operation. This increase was sustained until 170 h, after which the voltage decreased sharply. This rapid voltage decrease indicated cell failure due to short circuit. [26] However, the voltage of the Li metal with in situ LiF PL sample did not differ considerably from the initial value even after 350 h of operation. Figure 5.6f-g shows the AC impedance spectra of the Li/Li symmetrical cell. The equivalent circuit is shown in Figure 5.10. The bulk resistances of the bare Li metal and the Li metal with the in situ LiF PL samples were identical because the same electrolyte was used (Figure 5.10). The in situ LiF PL sample exhibited a lower charge transfer resistance than the bare Li metal sample because the artificial SEI layer was formed before cycling. LiF is electrochemically stable among SEI components; however it does not show high ionic conductivity ($<10^{-9}$ S cm^{-1}). As shown in Figure 5.10. The thickness of the LiF-PL is about 100 nm and this heterogenous layer is composed of polymeric materials including LiF (Figure 5.11). This means that there are many ways to pass Li cations. For this reason, only LiF formed on the surface does not dramatically reduce the charge transfer resistance. With the formation of the SEI layer, the electrode and electrolyte interfaces are stabilized, and charge transfer resistance is reduced. [27,28] It is assumed that a mixture structure with the LiF PL as the inner layer and the SEI as the outer layer formed on the Li metal surface. In this case, the resistance value of the in situ LiF PL sample was lower than that of the bare Li metal sample (Figure 5.6f-g). Thus,

the SEM images, voltage profiles, and AC impedance spectra confirmed that the in situ LiF PL effectively inhibited the volume expansion of Li metal and stabilized its surface.

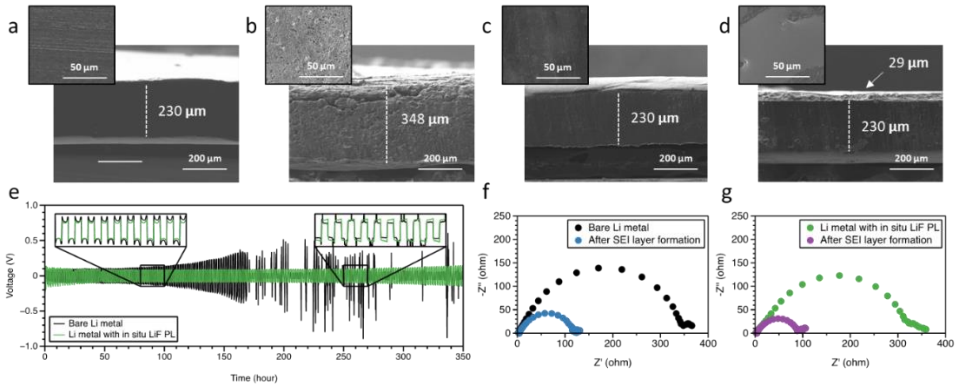

Figure 5.6 SEM images of surface and cross section of Li metal: (a) bare Li metal, (b) bare Li metal after 100 cycles with a current density of 1 mA cm^{-2}, (c) Li metal with in situ LiF PL, (d) Li metal with in situ LiF PL after 100 cycles with a current density of 1 mA cm^{-2}, (e) voltage profile of symmetrical cell test with bare Li metal (black) and Li metal with in situ LiF PL (green) at 1 mA cm^{-2}, and (f) AC impedance spectra of bare Li metal and Li metal with in situ LiF PL before and after SEI layer formation.

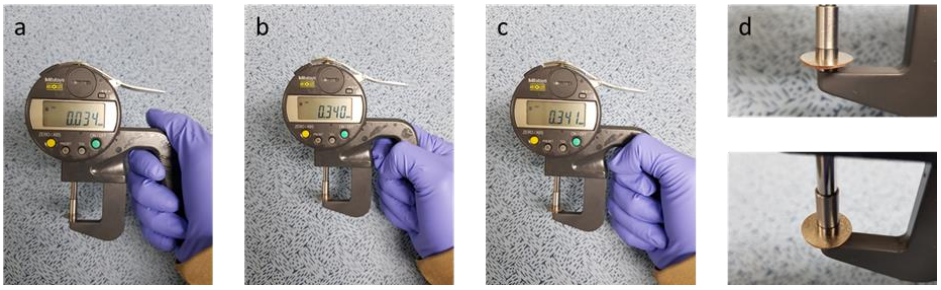

Figure 5.7 Picture of measuring thickness of in situ LiF PL. (a) Thickness of single layer of Cu/Li (b) Thickness of 10 layers of Cu/Li (c) Thickness of 10 layers of Cu/Li coated with in situ LiF PL (d) Images of measuring thickness of stacked Cu/Li

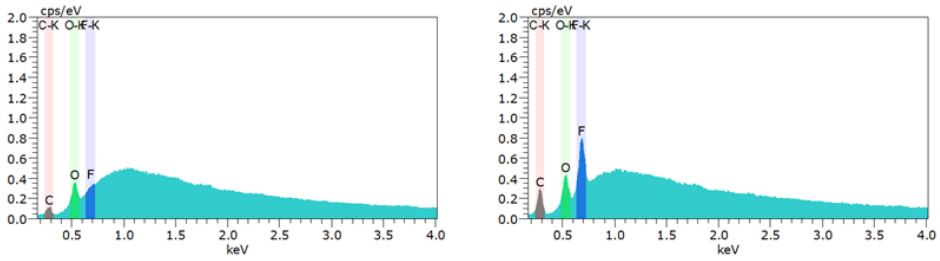

Figure 5.8 SEM-EDS analysis results of bare Li metal (left) and Li metal with in situ LiF PL (right)

Figure 5.9 Surface images of bare Li metal after 100 cycles (left) and Li metal with in-situ LiF PL after 100 cycles (right).

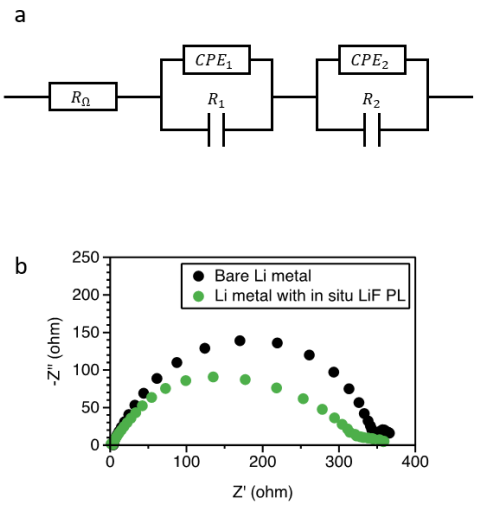

Figure 5.10 (a) Equivalent circuit of Li/Li symmetrical cell. AC impedance spectra of bare Li metal and Li metal with in situ LiF PL.

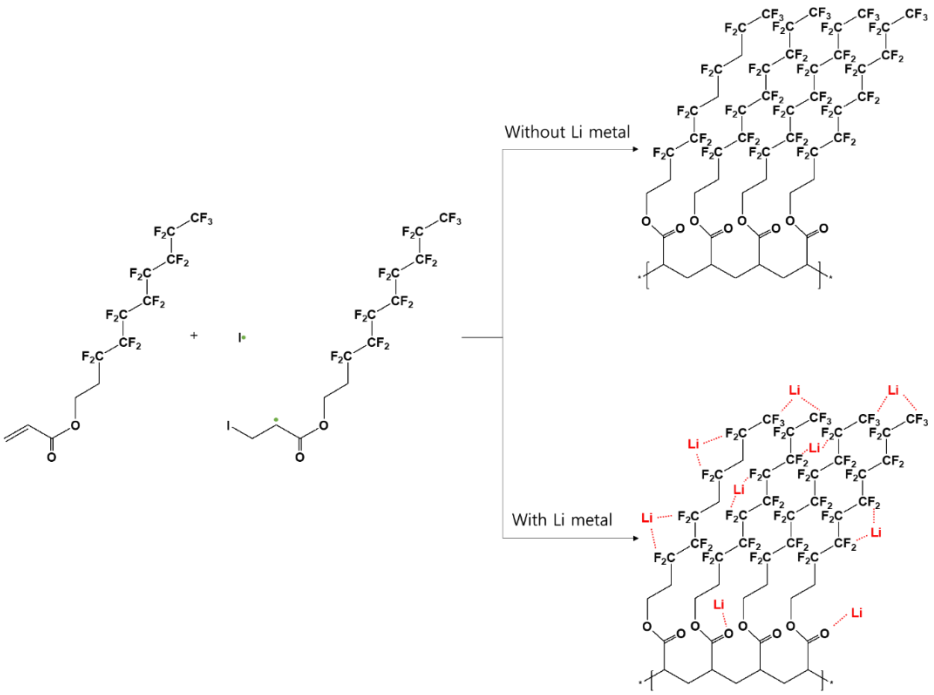

Figure 5.11 Polymerization mechanism of 2,2-(perfluorooctyl)ethyl acrylate

X-ray photoelectron spectroscopy (XPS) was performed using focused monochromatized Al Kα radiation (hν = 1486.7 eV) to verify the stability of the Li metal surface. To prevent the sample from exposure to air and moisture, XPS equipment connected to an argon-filled glove box was used. Figure 5.12 shows the results of the bare Li metal and the Li metal F-rich PL sample after 100 cycles. As shown in Figure 5.12a, the C1s spectrum of bare Li metal after 100 cycles exhibited peaks at 284.8, 286.8, and 290.3 eV corresponding to C–C/C–H, C–O, and CO_3^{2-} bonds, respectively. [18-20] These peaks are consistent with the expected formation of Li_2CO_3 and Li alkyl carbonate ($ROCO_2Li$) in the electrolyte decomposition reaction. [19] Most peaks in the C1s spectrum of the Li metal with in situ LiF PL sample after 100 cycles could be ascribed to the PL components of C–C/C–H, C–O, CF_n (290.7 eV), and O=C–O (289.1 eV) (Figure 5.12b). [22,23] The intensity of the C–O peaks increased relative to that obtained for the Li metal surface with in situ LiF PL without formation of the SEI layer owing to the decomposition of a few electrolytes. LiF and Li_xPF_y are produced when $LiPF_6$ is reduced. [29] LiF is chemically stable and stabilizes the surface by preventing dendrite growth. [13-15] For these reasons, LiF ratio is the most important parameter in the surface stabilization of Li metal. In the F1s spectra shown in Figure 5.12c-d, the peaks at 685.2, 687.0, and 688.3 eV represent LiF, Li_xPF_y, and $LiPF_6$, respectively. [19,29] For XPS analysis, the sample surfaces were washed with ethylene carbonate and dried in argon atmosphere. [11] However, $LiPF_6$ residues were present on the Li metal surface. In case of the bare Li metal sample, $LiPF_6$ was reduced to Li_xPF_y, and LiF. And Li_xPF_y ratio was higher than LiF. By contrast, because the LiF layer

was formed before electrolyte decomposition, the Li metal with in situ LiF PL suppressed the decomposition of $LiPF_6$, and thus, the proportion of Li_xPF_y was relatively low. In the Li1s spectra shown in Figure 5.12g-h, LiF, Li_2CO_3, and $ROCO_2Li$ can be observed, which were observed in the C1s and F1s spectra as well. After 100 cycles, the bare Li metal sample contained byproducts of electrolyte decomposition, whereas only the LiF peak was observed when the in situ LiF PL was applied. In the P2p spectra, $LiPF_6$ and phosphates were detected. In the case of bare Li metal, phosphate was detected dominantly. However, when the in situ LiF PL was applied, the intensity of phosphate was lower than that of the remainder of the $LiPF_6$ ratio. Figure 5.12i shows the atomic percentage after 100 cycles. C and O are distributed on the surface of the sample with the in situ LiF PL owing to the presence of crosslinked 2-(perfluorooctyl)ethyl acrylate. In case of the bare Li metal sample, C and O were generated through electrolyte decomposition in proportions higher than those in case of the sample with the in situ LiF PL. In the P2p spectra, the LiF ratio of the sample with the in situ LiF PL was 68.5% and that of the bare Li metal sample was 22.4%. Moreover, the P ratio of the sample with the in situ LiF PL was higher than that of the bare Li metal sample in terms of atomic percentage. Based on these values, we believe that the LiF content of the sample with the in situ LiF PL was considerably higher than that of the bare Li metal sample. The increase in Li metal thickness indicated by the SEM data was confirmed by the binding energy in the XPS data, and it was ascribed to electrolyte decomposition. It is understood that the F-rich PL effectively inhibited electrolyte decomposition.

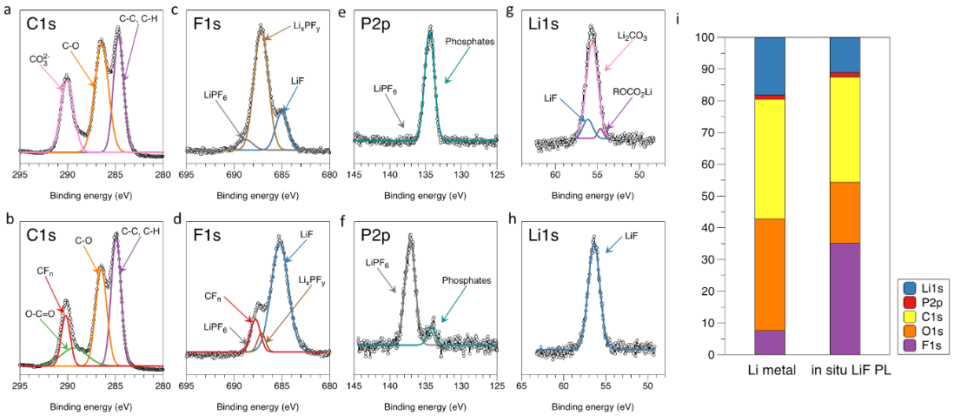

Figure 5.12 X-ray photoelectron spectroscopy (XPS) spectra of bare Li metal after 100 cycles (a, c, e, and g) and Li metal with in situ LiF PL after 100 cycles (b, d, f, and h). (i) The atomic percentages of bare Li metal and Li metal with in situ LiF PL after 100 cycles.

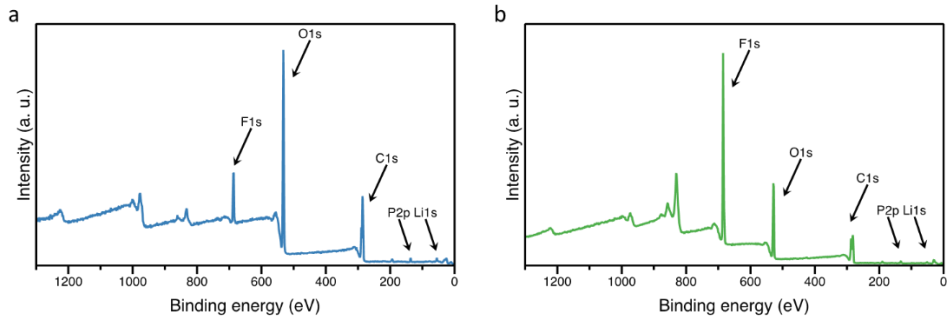

Figure 5.13 X-ray photoelectron spectroscopy (XPS) results of bare Li metal after 100 cycles (left) and Li metal with in situ LiF PL after 100 cycles (right).

5.2.4 Effect of in situ LiF protective layer for Li metal battery

Li metal anode is one part of the battery, and it is used together with a cathode in a real battery system. Therefore, we verify whether the in situ LiF PL on the anode works effectively in actual battery operation. To investigate the stability of the Li metal surface, a $LiFePO_4$/Li metal experiment was carried out using $LiFePO_4$, which is a stable cathode material, and the experiment results are shown in Figure 5.11. [11,30] Current densities of 0.2C, 0.5C, 1.0C, 2.0C, and 5,0C were applied for three cycles, and to confirm the recovery rate, the current density of 0.2C was applied for an additional three cycles. Figure 5.14a shows that the rate capabilities achieved using bare Li metal and Li metal with in situ LiF PL are almost similar. The same tendency is observed in the charge and discharge profile as well (Figure 5.14b-c). The areal capacity is also provided in Figure 5.15. Same as gravimetric capacity, bare Li metal and Li metal with the in situ LiF PL show 0.188 and 0.195 mA h cm^{-2} at 0.1C, respectively. The charging/discharging test was conducted for 1000 cycles to evaluate the long-term life of the cell. The cycle stability results at 1C are shown in Figure 5.14d. The initial capacities of both cells are similar. However, after 50 cycles, their capacities decreases gradually. After 100 cycles, the difference between the rates of capacity decrease of the cells with Li metal anode and Li metal with in situ LiF PL anode increases rapidly. As a result of charging and discharging for 1000 cycles at 1C, the capacity retention rates were 19.3% for bare Li metal and 45.9% for Li metal with in situ LiF PL, which is more than twice the rate for the cell with bare Li metal. Coulombic efficiency was maintained at around

the 100% level. Only in case of the bare Li metal anode, Coulombic efficiency decreased slightly after 250 cycles. The cycle results at 5C are shown in Figure 5.14e. As with the C-rate results, the initial capacities of the two cells are similar, but the capacities decline gradually. As a result, the capacity retention rate of the cell with the bare Li metal anode was 23.4%, whereas that of the Li metal anode with the in situ LiF PL was 52.1%. Thus, at 5C, the capacity retention rate of the Li metal anode with the in situ LiF PL was more than double that of the bare Li metal anode. Thus, the C-rate test did not show a capacity difference, but the Li metal anode with the in situ LiF PL showed excellent stability. To confirm the flexibility of the cell and the possibility of large-area application, a pouch sample was fabricated and subjected to a bending test. The pouch cell was assembled with the $LiFePO_4$/Li structure used in the cycle stability test. Figure 5.14f shows that the Li metal anode with the in situ LiF PL worked well. (Figure 5.16)

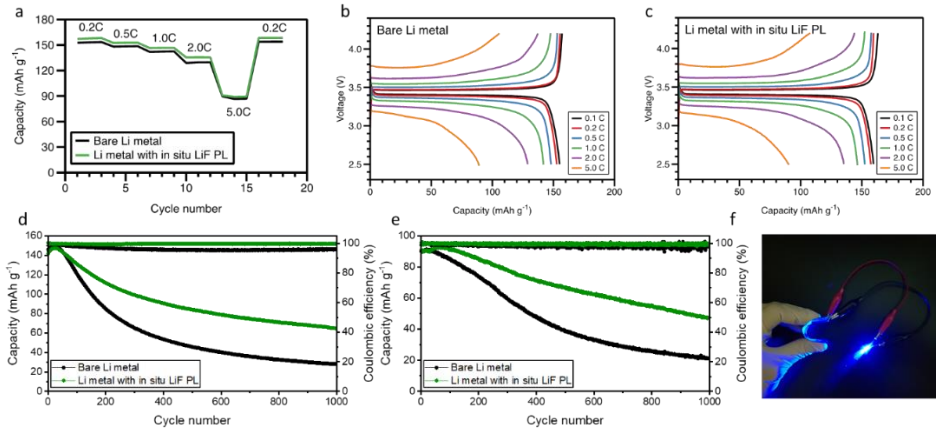

Figure 5.14 (a) The rate capability at various C-rates. Charge/discharge profiles of (a) bare Li metal and (b) Li metal with in situ LiF PL with $LiFePO_4$. The cycle capacity and Coulombic efficiency at (d) 1C and (e) 5C. (f) Image of flexibility test with pouch cell.

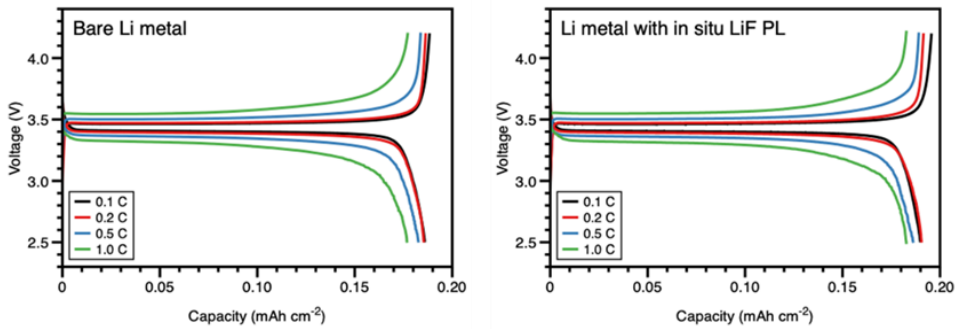

Figure 5.15 Charge/discharge profiles of (left) bare Li metal and (right) Li metal with in situ LiF PL with $LiFePO_4$.

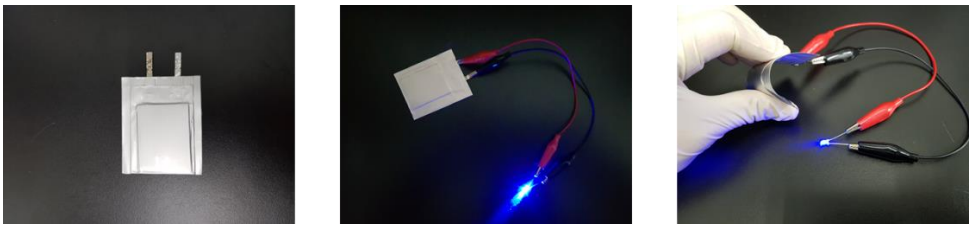

Figure 5.16 Images of pouch cell.

5.3 Conclusion

In summary, we proposed an in-situ LiF PL for Li metal. In this artificial SEI layer, LiF is formed by a simple process that involves thermal curing of F-rich material on the Li metal surface. Unlike the conventional method of embedding the LiF-rich layer in a polymer matrix, solvent and binder are not necessary. Moreover, the low thickness of the layer minimizes volumetric energy density loss, which is a fundamental disadvantage of the artificial SEI layer. The results of symmetrical cell tests demonstrated that the in situ LiF PL effectively inhibited the volumetric expansion of Li metal. Moreover, capacity retention rates after 1000 cycles of 45.9% and 52.1% were achieved in case of the Li metal anode with the in situ LiF PL at the current densities of 1C and 5C, respectively. We believe that this design will be a key factor in SEI stabilization.

5.4 Experimental details

PE separator, PVdF, and Super P were bought from Asahi Kasei Chemicals Corporation, Arkema, and MTI Korea, respectively. $LiFePO_4$ was obtained from Hanwa Chemicals. 1 M of $LiPF_6$ in ethylene carbonate (EC)/diethyl carbonate (DEC) (1:1 vol) was obtained from PANAX ETEC Co. Ltd and stored in an argon-filled glove box. Coin cells with the 2032-type configuration were assembled. The $LiFePO_4$ slurry was prepared by mixing $LiFePO_4$, Polyvinylidene fluoride (PVDF) and super P in the ratio of 8:1:1 with N-Methyl-2-pyrrolidone (NMP). 2.2 g of NMP was added based on 1 g of $LiFePO_4$ slurry to make proper viscosity. The slurry was coated on aluminum foil and then dried in a convection oven at 120 ℃ for 4 hours. This electrode pressed under 80% of original thickness with pressing machine. This pressed electrode was dried overnight in a vacuum oven at 120 ℃. Loading density of this electrode is 1.2 mg cm^{-2}.

5.5 References

[1] S. Chu and A. Majumdar, Nature, 2012, 488, 294–303.

[2] M. Armand, Nature, 2001, 414, 359–367.

[3] Lee, E. Paek, D. Mitlin and S. W. Lee, Chem. Rev., 2019, 119, 5416–5460.

[4] W. Xu, J. Wang, F. Ding, X. Chen, E. Nasybulin, Y. Zhang and J. G. Zhang, Energy Environ. Sci., 2014, 7, 513–537.

[5] B. Liu, J. G. Zhang and W. Xu, Joule, 2018, 2, 833–845.

[6] E. Peled and S. Menkin, J. Electrochem. Soc., 2017, 164, A1703–A1719.

[7] C. Han, Y. B. He, M. Liu, B. Li, Q. H. Yang, C. P. Wong and F. Kang, J. Mater. Chem. A, 2017, 5, 6368–6381.

[8] K. Liu, A. Pei, H. R. Lee, B. Kong, N. Liu, D. Lin, Y. Liu, C. Liu, P. chun Hsu, Z. Bao and Y. Cui, J. Am. Chem. Soc., 2017, 139, 4815–4820.

[9] X. B. Cheng, R. Zhang, C. Z. Zhao and Q. Zhang, Chem. Rev., 2017, 117, 10403–10473.

[10] H. Kim, Y. J. Gong, J. Yoo and Y. S. Kim, J. Mater. Chem. A, 2018, 6, 15540–15545.

[11] H. Kim, Y. S. Kim and J. Yoo, Sustain. Energy Fuels, 2020, 522–527.

[12] Y. Liu, D. Lin, P. Y. Yuen, K. Liu, J. Xie, R. H. Dauskardt and Y. Cui, Adv. Mater., 2017, 29, 1–8.

[13] J. Ko and Y. S. Yoon, Ceram. Int., 2019, 45, 30–49.

[14] J. Lang, Y. Long, J. Qu, X. Luo, H. Wei, K. Huang, H. Zhang, L. Qi, Q. Zhang, Z. Li and H. Wu, Energy Storage Mater., 2019, 16, 85–90.

[15] S. Choudhury and L. A. Archer, Adv. Electron. Mater., 2016, 2, 1–7.

[16] R. Xu, X. Q. Zhang, X. B. Cheng, H. J. Peng, C. Z. Zhao, C. Yan and J. Q. Huang, Adv. Funct. Mater., 2018, 28, 1–7.

[17] D. Lin, Y. Liu, W. Chen, G. Zhou, K. Liu, B. Dunn and Y. Cui, Nano Lett., 2017, 17, 3731–3737.

[18] G. Socrates, Infrared Characteristic Group Frequencies: Tables and Charts, 3rd Edition, Wiley & Sons: New York, 2004.

[19] J. Zheng, P. Yan, R. Cao, H. Xiang, M. H. Engelhard, B. J. Polzin, C. Wang, J. G. Zhang and W. Xu, ACS Appl. Mater. Interfaces, 2016, 8, 5715–5722.

[20] P. Shi, H. Zheng, X. Liang, Y. Sun, S. Cheng, C. Chen and H. Xiang, Chem. Commun., 2018, 54, 4453–4456.

[21] S. Leroy, F. Blanchard, R. Dedryvère, H. Martinez, B. Carré, D. Lemordant and D. Gonbeau, Surf. Interface Anal., 2005, 37, 773–781.

[22] C. S. Rustomji, Y. Yang, T. K. Kim, J. Mac, Y. J. Kim, E. Caldwell, H. Chung and Y. S. Meng, Science, 2017, 356, eaal4263

[23] R. Dedryvère, S. Leroy, H. Martinez, F. Blanchard, D. Lemordant and D. Gonbeau, J. Phys. Chem. B, 2006, 110, 12986–12992.

[24] N. Schulz, R. Hausbrand, C. Wittich, L. Dimesso and W. Jaegermann, J. Electrochem. Soc., 2018, 165, A833–A846.

[25] Q. Li, S. Zhu and Y. Lu, Adv. Funct. Mater., 2017, 27, 1–8.

[26] C.-P. Yang, Y.-X. Yin, S.-F. Zhang, N.-W. Li and Y.-G. Guo, Nat. Commun., 2015, 6, 8058.

[27] L. Yu, N. L. Canfield, S. Chen, H. Lee, X. Ren, M. H. Engelhard, Q. Li, J. Liu, W. Xu and J. G. Zhang, ChemElectroChem, 2018, 5, 761–769.

[28] X. B. Cheng, R. Zhang, C. Z. Zhao, F. Wei, J. G. Zhang and Q. Zhang, Adv. Sci., 2015, 3, 1–20.

[29] B. S. Parimalam and B. L. Lucht, J. Electrochem. Soc., 2018, 165, A251–A255.

[30] L. X. Yuan, Z. H. Wang, W. X. Zhang, X. L. Hu, J. T. Chen, Y. H. Huang and J. B. Goodenough, Energy Environ. Sci., 2011, 4, 269–284.

[31] Q. Wang, A. Sarkar, D. Wang, L. Velasco, R. Azmi, S. S. Bhattacharya, T. Bergfeldt, A. Düvel, P. Heitjans, T. Brezesinski, H. Hahn and B. Breitung, Energy Environ. Sci., 2019, 12, 2433–2442.

Chapter 6 Conclusion

The findings above suggest three methods to stabilize Li metal surfaces.

The first method is to apply a three-dimensional mesh structure to a Li metal surface. This three-dimensional mesh structure relieves the force from volume expansion and disperses Li ion flux, thereby preventing growth of Li dendrite. As a result, the Li metal battery with three-dimensional mesh structure shows improved cycle performance. (Chapter 3)

The second method is to form a polymer layer on the Li metal surface through thermal curing. Due to an ethylene oxide units consisting, it interacts with the Li ion transfer and suppresses volume expansion of Li metal. Electrochemical experiments have confirmed that this protective polymer layer stabilizes the Li metal surface. In addition, any energy density reduction due to the protective layer is minimized thanks to the low mass density and high flexibility of the polymer. (Chapter 4)

The third method is to form a lithium fluoride (LiF) layer on the Li metal surface using F-rich material. LiF is the main component of the SEI layer with a high electrochemical stability. The layer is manufactured through a very simple process, unlike the complex processes published in previous studies. This protective layer shows excellent properties when implemented in the context of a Li metal battery. (Chapter 5)

The studies presented in this paper have progressed in a direction that minimizes the loss of energy density by implementing the processes that keep the battery

additives simpler, thinner, and lighter. These methods suggest the possibility of Li metal anode commercialization.

List of publications

- **Hyunjin Kim**, Youn Sang Kim, and Jeeyoung Yoo, “An in situ formed LiF protective layer on a Li metal anode with solvent-less cross-linking”
  Sustainable Energy & Fuels, *4, 3282-3287 (2020)*
- Yong Jun Gong, Jung Woon Heo, Hakji Lee, **Hyunjin Kim**, Jinil Cho, Seonmi Pyo, Heejun Yun, Heebae Kim, Sang Yoon Park, Jeeyoung Yoo, and Youn Sang Kim, “Nonwoven rGO Fiber-Aramid Separator for High-Speed Charging and Discharging of Li Metal Anode”
  Advanced Energy Materials*, 2001479-2001479 (2020)*
- **Hyunjin Kim**, Youn Sang Kim, and Jeeyoung Yoo, “Solventless Thermal Crosslinked polymer protective layer for high stable lithium metal batteries”
  Sustainable Energy & Fuels, *4, 522-527 (2020)*
- Yong Jun Gong, **Hyunjin Kim**, Gayeong Yoo, Jinil Cho, Seonmi Pyo, Yong Hyun Cho, Jeeyoung Yoo, and Youn Sang Kim, “Ni-Particle-Embedded Bilayer Gel Polymer Electrolyte for Highly Stable Lithium Metal Batteries”
  ACS Applied Energy Materials, *2, 11, 2310-8318 (2019)*
- **Hyunjin Kim**, Yong Jun Gong, Jeeyoung Yoo and Youn Sang Kim, “Highly stable lithium metal battery applied three-dimensional mesh structure interlayer.”
  Journal of Materials Chemistry A, *6, 15540-15545 (2018)*
- Chang Su Yeo, **Hyunjin Kim**, Taekyung Lim, Hyuk Joon Kim, Sanghun Cho, Kang Rae Cho, Youn Sang Kim, Min Kyoon Shin, Jeeyoung Yoo, Sanghyun

Ju, and Sang Yoon Park, “Copper-embedded reduced graphene oxide fibers for multi-sensors”

Journal of Materials Chemistry C, *5, 12825-12832 (2017)*

- Sanghun Cho, Yong-keon Ahn, Zhenxing Yin, Duck-Jae You, **Hyunjin Kim**, Yuanzhe Piao, Jeeyoung Yoo and Youn Sang Kim, “Synthesis of copper oxide/graphite composite for a high-performance rechargeable battery anode”

  Chemistry - A European Journal, *23, 1-8 (2017)*

- Duck-Jae You, Zhenxing Yin, Yong-keon Ahn, Sanghun Cho, **Hyunjin Kim**, Dalwoo Shin, Jeeyoung Yoo, and Youn Sang Kim, “A high-performance polymer composite electrolyte embedded with ionic liquid for all solid lithium based batteries operating at ambient temperature”

  Journal of Industrial and Engineering Chemistry, *52, 1-6 (2017)*

- Yong-keon Ahn, Bokyung Kim, Jieun Ko, Duck-jea You, Zhenxing Yin, **Hyunjin Kim**, Dalwoo Shin, Sanghun Cho, Jeeyoung Yoo and Youn Sang Kim, “All Solid Flexible Supercapacitor Operating at 4V with Cross-linked Polymer-ionic Liquid Electrolyte”

  Journal of Materials Chemistry A, *4, 4386-4391, (2016)*

- Yong-keon Ahn, Junwoo Park, Dalwoo Shin, Sanghun Cho, Si Yun Park, **Hyunjin Kim**, Jeeyoung Yoo and Youn Sang Kim, “Enhanced Electrochemical Capabilities of Lithium Ion Batteries by Structurally Ideal Anodic Aluminum Oxide Electrode”

  Journal of Materials Chemistry A, *3, 10715-10719, (2015)*

요약 (국문초록)

안정한 리튬 금속 전지를 위한 리튬 금속 표면 제어

김현진
융합과학부 나노융합전공
융합과학기술대학원
서울대학교

배터리는 현대사회의 핵심 기술이다. 우리가 일상생활에서 흔히 사용하는 스마트폰, 스마트워치, 노트북에서부터 전기 자동차에 이르기까지 대부분의 소자에 배터리를 사용하고 있다. 소비자는 한번 충전했을 때 더 오랜 시간 사용하기를 원하는데 배터리 기술에서 용량은 가장 중요한 부분을 차지한다. 배터리는 음극과 양극, 전해질과 분리막으로 나눌 수 있는데, 용량을 높이기 위해서는 음극과 양극에서 높은 용량을 갖는 전극 물질을 사용해야 한다. 리튬 금속은 음극 물질 중에서도 이론 용량이 가장 높고 전기화학 전위가 낮아 차세대 고용량 전지의 물질로 각광을 받고 있다. 하지만 리튬 금속의 표면 안정성 문제는 상업화의 걸림돌이 되어 여전히 흑연 기반의 음극 물질에

머무르고 있다. 이 논문에서는 리튬 금속 표면을 제어하기 위한 세 가지 연구를 다룬다.

첫 번째 연구는 리튬 금속 표면에 스테인리스강 성분의 3 차원 구조를 적용하는 것이다. 3 차원 구조는 리튬 금속 표면에서 부피 팽창하는 힘을 완화시켜주고 전류 밀도를 분산시켜 주기 때문에 리튬이 수지상으로 성장하는 것을 막아준다. 그리고 전자 이동 경로를 제공하여 높은 쿨롱 효율을 유지할 수 있도록 도와준다. 이를 리튬 금속 전지를 제작하여 적용했을 때 향상된 수명 특성을 보여주었다.

두 번째 연구는 열 경화를 통해 리튬 금속 표면에 고분자 층을 형성하는 것이다. 사용한 고분자는 ethylene oxide unit 을 갖고 있기 때문에 리튬 금속 표면에서 리튬 이온을 전달해 주는 역할과 동시에 리튬 금속의 부피 팽창을 억제해 준다. 전기화학 특성 실험을 통해 제작된 고분자 보호막 층이 리튬 금속 표면을 안정화 시켜준다는 것을 확인하였다. 얇고 가벼운 고분자 층을 사용하기 때문에 전지 시스템에서 에너지 밀도 손실을 최소화로 줄여준다.

세 번째 연구는 열 경화를 통해 리튬 표면에 lithium fluoride (LiF) 층을 부여하는 것이다. LiF 는 solid electrolyte interphase (SEI) 층의 주요 구성 성분으로 전기화학적으로 가장 안정하기 때문에 리튬 금속에 LiF 층이 형성되면 SEI 층을 보다 안정하게 유지시킬 수 있다. LiF 를 리튬 금속 표면에 적용하는 방법이 복잡한 이전 연구와는 다르게 리튬 금속 표면에 보호막 층을 코팅하여 열을 가하기만 하면 형성되는 매우 간단한 방식으로 제작되었다. 이 보호막 층은 리튬 금속 전지에서 우수한 특성을 보여준다.

이 논문에서 제시된 연구들은 공정이 간단하면서도 더 얇고 더 가볍게 제작되어 보호막의 근본적인 단점이라고 할 수 있는 에너지 밀도 손실을 최소화하는 방향으로 실험이 진행되었다. 이 기술들은 리튬 금속 음극을 상용화할 수 있는 가능성을 제시해 준다.

주요어 : 리튬 금속 음극, 리튬 금속 전지, 보호막, 인공 고체전해질 계면 층

학 번 : 2014-24876